MAGNETIC RESONANCE IN CHEMISTRY
Magn. Reson. Chem. 2007; **45**: S247–S260
Published online in Wiley InterScience
(www.interscience.wiley.com) DOI: 10.1002/mrc.2160

MRC

Investigation of finite-pulse radiofrequency-driven recoupling methods for measurement of intercarbonyl distances in polycrystalline and membrane-associated HIV fusion peptide samples

Zhaoxiong Zheng, Wei Qiang and David P. Weliky*

Department of Chemistry, Michigan State University, East Lansing, MI 48824, USA

Received 12 July 2007; Revised 24 October 2007; Accepted 2 November 2007

Two finite-pulse radiofrequency-driven recoupling (RFDR) methods were compared and applied to the measurement of 3–6 Å ^{13}CO–^{13}CO distances in polycrystalline and membrane-associated HIV fusion peptide (HFP) samples. The RFDR methods were based on π pulses and were relatively straightforward to implement and insensitive to pulse imperfections. The two tested methods were: (i) constant-time double-quantum buildup with finite pulses (fpCTDQBU) for which the pulse sequence maintained a constant transverse relaxation period while allowing a variable period of dipolar dephasing; and (ii) constant-time finite-pulse rf-driven recoupling (fpRFDR-CT) for which the duration of transverse relaxation increased with increasing dephasing period. The fpRFDR-CT method yielded higher signal-to-noise and an accurate determination of a ~5 Å intercarbonyl distance was made in a crystalline peptide which had $T_2 \approx 55$ ms. In some contrast, the HFP samples had $T_2 \approx 15$ ms and the fpRFDR-CT data were dominated by transverse relaxation. Examination of the fpCTDQBU sequence showed: (i) the most rapid signal buildup was obtained with application of one ^{13}C π pulse per rotor period rather than one ^{13}C π pulse per multiple rotor periods and (ii) the data were insensitive to ~15 ppm transmitter offset and to ~5° variation of π pulse nutation angle. For HFP samples which were ^{13}CO labeled at a single residue, analyses of the fpCTDQBU data were interpreted with a model of mixed parallel and antiparallel β-strand arrangements in the *N*-terminal region of HFP and loss of parallel β-sheet structure in the *C*-terminal region of HFP.

KEYWORDS: NMR; ^{13}C; solid-state; dipolar coupling; RFDR; HIV; fusion peptide; membrane fusion

INTRODUCTION

Over the past 20 years, solid-state nuclear magnetic resonance (NMR) has provided structural information about noncrystalline biological solids such as membrane-associated peptides and proteins, and amyloid fibrils and intermediates.[1–3] A significant number of published studies were measurements of ^{13}C–^{13}C homonuclear dipolar recoupling (d) under magic angle spinning (MAS) with which sharp NMR signals could be observed. The relationship between the internuclear distance r and d is $r = (7740/d)^{1/3}$ where r and d have Å and Hz units, respectively. A variety of methods have been developed for measurement of these couplings including R^2, RFDR, SEDRA, DRAMA, HORROR, DRAWS, C7, post-C7, CMR7, SC14$_4^5$, R14$_2^6$, and SR26.[4–16]

This article describes investigation of the radiofrequency-driven recoupling (RFDR) or SEDRA method in which ^{13}C transverse magnetization evolves under trains of ^{13}C π pulses with one pulse per integral number of rotor periods.[14–16] The RFDR setup is straightforward and rapid because the ^{13}C pulses are π pulses with quadrature phases. Effects of ^{13}C transverse relaxation may be reduced in constant-time (*CT*) versions of RFDR in which there are a constant number of π pulses and a single total duration of ^{13}C evolution for all dipolar dephasing times.[17,18] Use of ^{13}C π pulses that are an appreciable fraction of a rotor period is an additional modification and for such finite-pulse RFDR (fpRFDR) sequences, the average Hamiltonian is proportional to the static homonuclear dipolar coupling Hamiltonian.[19] The fpRFDR technique is relatively insensitive to ^{13}C chemical shifts and ^{13}C chemical shift anisotropies (CSAs) including tensor orientations and is well-suited to distance measurements in carbonyl (^{13}CO)-labeled samples that are relatively inexpensive to prepare.[19–22] Although fpRFDR was originally developed with rotors of small diameter and volume for which the MAS frequency was >20 kHz, fpRFDR has also been applied at the ~10 kHz MAS frequencies achievable with larger volume rotors.[22,23] Higher signals may be obtained with these rotors for samples that are limited

*Correspondence to: David P. Weliky, Department of Chemistry, Michigan State University, East Lansing, MI 48824, USA.
E-mail: weliky@chemistry.msu.edu

in concentration such as membrane-associated peptides and proteins.

This paper considers two variants of the fpRFDR sequence. For the constant-time double-quantum buildup with finite pulses (fpCTDQBU) method, the ^{13}C π pulse train was divided into two parts, the first of which generated either ^{13}C dipolar evolution or dipolar refocusing, and the second of which generated dipolar refocusing only.[17,22] The refocusing was achieved with solid echoes and selection of either evolution or refocusing was controlled by the phase of a ^{13}C $\pi/2$ pulse. The sum of the durations of the first and second periods was always a single *CT*. The second variant, constant-time finite-pulse rf-driven recoupling (fpRFDR-CT), contained WAHUHA periods for dipolar refocusing.[20,21,24] Relative to solid echoes, the WAHUHA approach may result in higher signal because of better dipolar refocusing.[25,26]

This paper provides some comparison between the fpCTDQBU and fpRFDR-CT methods in both polycrystalline model compounds and membrane-associated HIV fusion peptide (HFP) samples. An investigation was made of the necessity for *CT* in measurement of structurally interesting $r \sim 5$ Å distances with $d \sim 60$ Hz. In addition, comparison was made between a version of fpCTDQBU with one ^{13}C π pulse per two rotor periods and a version with one ^{13}C π pulse per rotor period.[22] The latter version could generate more rapid dipolar evolution and permitted shorter durations of *CT* with concomitant reduced transverse relaxation and higher signals. Investigations by experiment and simulation were also made of effects of transmitter offsets (Δ) and pulse nutation angle (θ) errors on fpCTDQBU data and the derived ^{13}C–^{13}C distances.

In addition to the examination of the fpRFDR techniques, this paper also includes application of fpCTDQBU for determination of β-strand arrangements in membrane-associated HFP samples. The human immunodeficiency virus (HIV) is surrounded by a membrane that the virus obtains from an infected cell during viral budding. Infection of a new cell begins with joining or 'fusion' of the viral and host cell membranes leading to deposition of the viral nucleocapsid in the host-cell cytoplasm.[27,28] For HIV, fusion is catalyzed by the gp41 integral membrane protein of the virus.[29] The gp41 protein contains an ~20-residue *N*-terminal HFP domain and an important step in fusion is binding of the HFP to the target cell membrane.[30] Peptides containing the HFP sequence catalyze fusion between vesicles and observation of similar mutation–fusion activity relationships for HIV-induced and HFP-induced fusion suggests that the HFP can serve as a useful fusion model.[31–33]

The membrane-associated structure of HFP has been studied with a variety of biophysical methods including solid-state NMR. Both helical and β-strand conformations have been observed with a larger β-strand fraction in cholesterol-containing membranes.[22,32,34,35] The β-strand structure may have a biological relevance, because the membranes of host cells of HIV contain ~30 mol% cholesterol.[36,37] Earlier solid-state NMR measurements showed that the β strands formed hydrogen-bonded aggregates and indicated a mixture of parallel and antiparallel β-strand arrangements.[38]

During the past five years, there has been progress in synthesis of HFPs that reflect more closely HFP in gp41. In one effort, a longer 'N70' peptide was made which contained the first 70 residues of gp41.[39] Relative to the 23-residue HFP, the N70 construct induced vesicle fusion at much lower peptide concentrations. In addition, high-resolution structures of gp41 constructs which lacked the HFP showed trimeric protein and suggested that at least three HFPs interact with the membrane with their *C*-termini in close proximity.[28,40–44] These structures motivated the synthesis of the chemically cross-linked 'HFPtr' construct that contained three HFP strands.[45,46] The significance of trimerization was indicated by a rate of vesicle fusion induced by HFPtr that was as much as 40 times greater than the rate induced by single-strand 'HIV fusion peptide monomer (HFPmn)'. One structural hypothesis for the increased fusion of N70 and HFPtr is formation of predominant parallel rather than mixed parallel and antiparallel β-strand arrangements. A parallel arrangement would place the most apolar *N*-terminal regions of HFP strands close to one another and the resultant large apolar volume would cause greater perturbation of the membrane and more rapid fusion. Analysis of infrared spectra of membrane-associated N70 supported a parallel strand arrangement.[47]

For peptides in amyloid fibrils, strand arrangements have been elucidated using measurements of interpeptide ^{13}C–^{13}C dipolar couplings in samples containing peptides with a single backbone ^{13}CO label.[21,48] For an in-register parallel strand arrangement, the ^{13}CO–^{13}CO $r \approx 4.8$ Å with corresponding $d \approx 70$ Hz while an antiparallel arrangement would typically have greater r and much smaller d. This approach is the conceptual basis for the investigation of strand arrangements in membrane-associated HFP in this paper.

EXPERIMENTAL

Materials

Resins and amino acids were purchased from Advanced Chemtech (Louisville, KY, USA), Calbiochem-Novabiochem (La Jolla, CA, USA) and Peptides International (Louisville, KY, USA). Labeled amino acids were purchased from Icon Services (Summit, NJ, USA) and were fluorenylmethoxycarbonyl (FMOC)-protected using literature methods.[49,50] The FMOC-1-^{13}C glycine was purchased from Sigma-Aldrich (St Louis, MO, USA). The 1,2-di-*O*-tetradecyl-*sn*-glycero-3-phosphocholine (DTPC), 1,2-di-*O*-tetradecyl-*sn*-glycero-3-[phospho-*rac*-(1-glycerol)] (sodium salt) (DTPG), and cholesterol were purchased from Avanti Polar Lipids (Alabaster, AL, USA). The *N*-(2-hydroxyethyl)piperazine-*N*′-2-ethanesulfonic acid (HEPES) was obtained from Sigma-Aldrich (St Louis, MO, USA). The buffer solution used in the study contained 5 mM HEPES (pH 7.0) with 0.01% NaN_3.

N-acetyl-L-leucine (NAL) and glycyl-L-phenylalanyl-L-phenylalanine (GFF)

Unlabeled *N*-acetyl- L -leucine (NAL) and unlabeled glycyl-L-phenylalanyl-L-phenylalanine (GFF) were purchased from ICN (Aurora, OH, USA) and Sigma-Aldrich (St Louis, MO, USA), respectively. Doubly 1-^{13}C, N-^{13}C labeled NAL

DOI: 10.1002/mrc

and GFF with ^{13}CO labels at Gly-1 and Phe-3 were synthesized as setup compounds.[22] Solution ^{1}H and ^{13}C NMR confirmed the identity, purity and labeling of the compounds. A polycrystalline D-NAL sample was prepared by aqueous dissolution of a 1 : 9 mixture of doubly labeled : unlabeled material followed by evaporation of the water and crystallization. The polycrystalline mixture of doubly labeled and unlabeled GFF (D-GFF) sample was similarly prepared except that the doubly labeled : unlabeled ratio was 1 : 49. The intramolecular labeled ^{13}C–^{13}C distances in crystalline D-NAL and in crystalline D-GFF are 3.07 and 5.40 Å, respectively.[51,52] The purpose of the dilution was to increase the average distance between labeled molecules so that the intermolecular ^{13}C–^{13}C couplings between labeled molecules could be neglected. The dilution in the D-GFF sample was greater than in the D-NAL sample because the intramolecular ^{13}C–^{13}C distance was larger in the D-GFF sample and the experiments, therefore, probed larger intermolecular distances.

Fusion peptides

'HFPmn-F8' was synthesized as a *C*-terminal amide using a Model 431A peptide synthesizer (ABI, Foster City, CA, USA) equipped for FMOC solid-phase chemistry. The amino acid sequence of HFPmn-F8 was AVGIGALFLGFLGAAGSTMGARS that corresponded to the 23 *N*-terminal residues of the LAV_{1a} strain of the HIV gp41 envelope fusion protein. HFPmn-F8 contained a ^{13}CO label at Phe-8. The purified yield of HFPmn was ~85%.

Syntheses of 'fusion peptide trimer (HFPtr)-A6' and 'HFPtr-A15' began with chemical synthesis of a HFP with sequence AVGIGALFLGFLGAAGSTMGARSWKKKKKCA$_\beta$ and a fusion peptide with sequence (AVGIGALFLGFLG AAGSTMGARSWKKKKKC)(AVGIGALFLGFLGAAGST MGARSWKKKKKKA$_\beta$) where A$_\beta$ refers to β-alanine. The sequences in parentheses represented individual peptide strands and there was a chemical bond between the CO of the underlined cysteine and the NH of the side chain of the underlined lysine.[46] The purified yield for this peptide was ~45%. A HFPtr was prepared by cysteine cross-linking of these two peptides and the purified yield of the cross-linking step was ~35%.[45] The nonnative *C*-terminal lysines greatly improved aqueous solubility and the nonnative tryptophan served as a 280 nm chromophore for peptide quantitation. HFPtr-A6 was ^{13}CO labeled at Ala-6 on each strand and HFPtr-A15 was ^{13}CO labeled at Ala-15 on each strand.

HFPs were purified with reverse-phase high-performance liquid chromatography (HPLC) using a preparative C_{18} column (Vydac, Hesperia, CA, USA) and a water–acetonitrile gradient containing 0.1% TFA. Mass spectroscopy was used for peptide identification and the peptide purity was estimated to be >95% based on the mass spectra.

Lipid preparation

The membranes for the HFP samples were prepared using a 'PC/PG/CHOL' mixture that contained DTPC and DTPG lipids and cholesterol in an 8 : 2 : 5 mol ratio. PC/PG/CHOL served as a simple model of the membrane composition of host cells of HIV and had phosphatidylcholine as the major lipid headgroup as well as a cholesterol : lipid ratio similar to these membranes.[36,37] Unlike host cell membranes, PC/PG/CHOL contained ether-linked rather than ester-linked lipids to eliminate natural abundance lipid ^{13}CO signals that would have complicated the data analysis. Previous experiments have shown that the membrane-associated HFP conformation was not affected by replacement of ester-linked lipids with ether-linked lipids.[22]

Lipid and cholesterol powders were dissolved together in chloroform. The chloroform was removed under a stream of nitrogen followed by overnight vacuum pumping. Lipid dispersions were formed by addition of 5 mM pH 7.0 HEPES buffer followed by homogenization with 10 freeze-thaw cycles. Large unilamellar vesicles (LUVs) were prepared by extrusion through a filter with 100 nm diameter pores.

Solid-state NMR sample preparation

Polycrystalline D-NAL (~260 total μmol with ~26 μmol doubly labeled compound) and D-GFF (~140 total μmol with ~2.8 μmol doubly labeled compound) were ground before being packed in 4 mm diameter MAS NMR rotors.

For the membrane-associated HFP samples, 0.1–0.2 μmol HFPtr or 0.6 μmol HFPmn was dissolved in ~2 ml of 5 mM HEPES buffer and LUVs (~30 μmol total lipid + cholesterol) were prepared in ~2 ml of buffer. The peptide and LUV solutions were mixed and kept at room temperature for 45–60 min followed by ultracentrifugation at 35 000 rpm for 5 h at 4 °C. The peptide/lipid pellet formed after ultracentrifugation was transferred to a 4 mm diameter MAS NMR rotor by spatula. Unbound HFPs did not pellet under these conditions and there was approximately quantitative incorporation of HFP into the membrane.[35,38]

Solid-state NMR spectroscopy

Experiments were done on a 9.4 T spectrometer (Varian Infinity Plus, Palo Alto, CA, USA) using a MAS probe in double resonance ^{13}C/^{1}H configuration. The NMR detection channel was tuned to ^{13}C at 100.8 MHz and the decoupling channel was tuned to ^{1}H at 400.8 MHz. ^{13}C shifts were externally referenced to the methylene resonance of adamantane at 40.5 ppm. Spacers were used to restrict samples to the central 2/3 rotor volume (~40 μl) in which radio frequency (rf) field variation was less than 10%.

Experiments were performed at −50 °C rather than room temperature in order to achieve more efficient cross-polarization (*CP*) and greater signal per ^{13}C nucleus. There were similar ^{13}C backbone chemical shifts at both low temperature and room temperature, suggesting that cooling the sample does not cause significant peptide structural changes.[53] The ^{1}H and ^{13}C pulse lengths were approximately obtained by direct pulsing adamantane and the *CP* matching condition was obtained by running ramped *CP* on D-NAL. Calibration of the ^{1}H $\pi/2$, ^{13}C $\pi/2$, and ^{13}C π pulses was done with the *CP* 'Z-filter' sequence ($CP - \pi/2 - \tau - \pi - acquisition$) run on the D-NAL sample.

For both the fpCTDQBU and fpRFDR-CT experiments, typical parameters included 12 000 ± 2 Hz MAS frequency, ramped 50–60 kHz ^{13}C and constant 65 kHz ^{1}H fields during the 3 ms *CP* period, 20.5 kHz ^{13}C π pulses, 50 kHz

DOI: 10.1002/mrc

^{13}C $\pi/2$ pulses, continuous-wave (CW) ^{1}H decoupling of 95 and 60 kHz during the *fpRFDR* and acquisition periods, respectively, and 1.5 s recycle delay. Decoupling fields greater than 100 kHz led to arcing in the probe. Except when studying effects of transmitter offset, the ^{13}C transmitter was set to 172.4 ppm for D-NAL, 175.5 ppm for D-GFF, 166.2 ppm for membrane-associated HFPmn-F8 and HFPtr-A6, and 158.4 ppm for membrane-associated HFPtr-A15. A larger transmitter offset was used for the HFPtr-A15 sample because of the larger ^{13}CO linewidth in this sample.

fpCTDQBU spectroscopy

Figure 1(a) displays the fpCTDQBU sequence that had the form $CP_{\zeta+\pi/2} - (fpRFDR)_L - \pi/2_{\zeta}\ \pi/2_x - (fpRFDR)_M - \pi/2_{-x}\ \pi/2_y - (fpRFDR)_N - acquisition$ where L, M, and N were integers and $(fpRFDR)_L$, $(fpRFDR)_M$, and $(fpRFDR)_N$ had durations $L\tau_R$, $M\tau_R$, and $N\tau_R$ with τ_R being the duration of a rotor cycle. Transverse ^{13}C magnetization was generated during the *CP* period, evolved during the *fpRFDR* periods, and was detected during the acquisition period. Both $M = L + N$ and $L + M + N$ were held constant for a data set and the latter expression resulted in a *CT* period of duration $(L + M + N)\tau_R$ for evolution of the transverse ^{13}C magnetization. The evolution time can be understood as consecutive periods of duration $2L\tau_R$ and $2N\tau_R$ with the $\pi/2_{\zeta}\ \pi/2_x$ pulse pair at the midpoint of the first period and the $\pi/2_{-x}\pi/2_y$ pulse pair at the midpoint of the second period. As will be explained below, the $\pi/2_{\zeta}\ \pi/2_x(\zeta = y, -y)$ and $\pi/2_{-x}\pi/2_y$ pulse pairs refocused the ^{13}C evolution due to ^{13}C–^{13}C dipolar coupling during the $2L\tau_R$ and $2N\tau_R$ periods, respectively, while the $\pi/2_{\zeta}\ \pi/2_x(\zeta = x, -x)$ pulse pair did not refocus ^{13}C dipolar evolution during the $2L\tau_R$ period. For $\pi/2_{\zeta}\ \pi/2_x$ $(\zeta = x, -x)$ pulse pairs, the $2L\tau_R$ period was therefore the dipolar evolution period and was denoted as τ. The value of τ was varied by incrementing L and decrementing N by the same number.

For each τ, free induction decays (FIDs) with $\zeta = x, y, -x, -y$ were recorded. The S_0 signal (no ^{13}C–^{13}C dipolar evolution during τ) was formed from addition of the FIDs with $\zeta = y$ and $-y$ while the S_1 signal (^{13}C–^{13}C dipolar evolution during τ) was formed with addition of the FIDs with $\zeta = x$ and $-x$. The $2N\tau_R$ period provided an additional constraint of total CT for transverse ^{13}C relaxation that was independent of τ for both the S_0 and S_1 data. Two versions of the fpCTDQBU sequence were tested and were denoted 'one-π-per-τ_R' and 'one-π-per-$2\tau_R$' (Fig. 1(b), (c)). These versions differed during the *fpRFDR* periods in having one ^{13}C π pulse per rotor cycle or one ^{13}C π pulse per two rotor cycles, respectively. XY-8 phase cycling was used for the ^{13}C π pulses and L, M, and N were integral multiples of 8 or 16 for the one-π-per-τ_R and one-π-per-$2\tau_R$ versions, respectively.[54]

The effect of the $\pi/2$ pulse pairs on ^{13}C dipolar evolution can be understood with average Hamiltonian theory.[25,55,56] The *fpRFDR* periods refocus ^{13}C chemical shift evolution and result in an average dipolar Hamiltonian between two ^{13}C spins that is proportional to the static dipolar Hamiltonian and has spin operator dependence:[19]

$$H_{zz} = 3I_{z1}I_{z2} - \boldsymbol{I}_1.\boldsymbol{I}_2 \quad (1)$$

where $\boldsymbol{I}_1$ and $\boldsymbol{I}_2$ are the nuclear spin operators of ^{13}C spins 1 and 2. For $\zeta = -y$, the propagator during the τ period is represented by:

$$U(\tau) = e^{-(DL\tau_R)H_{zz}}e^{(i\pi/2)I_x}e^{(-i\pi/2)I_y}e^{-(DL\tau_R)H_{zz}} \quad (2)$$

where D is the effective angular dipolar frequency. Equation (2) is evaluated as follows:

$$\begin{aligned} U(\tau) &= e^{(i\pi/2)I_x}e^{-(i\pi/2)I_x}e^{-(DL\tau_R)H_{zz}}e^{(i\pi/2)I_x}e^{(-i\pi/2)I_y}e^{-(DL\tau_R)H_{zz}} \\ &= e^{(i\pi/2)I_x}e^{-(DL\tau_R)H_{yy}}e^{(-i\pi/2)I_y}e^{-(DL\tau_R)H_{zz}} \end{aligned} \quad (3)$$

where $H_{yy} = 3I_{y1}I_{y2} - \boldsymbol{I}_1.\boldsymbol{I}_2$. The second and third terms commute with one another and can be interchanged to yield:

$$U(\tau) = e^{(i\pi/2)I_x}e^{(-i\pi/2)I_y}e^{-(DL\tau_R)H_{yy}}e^{-(DL\tau_R)H_{zz}} \quad (4)$$

Incorporation of the conditions that H_{xx}, H_{yy}, and H_{zz}

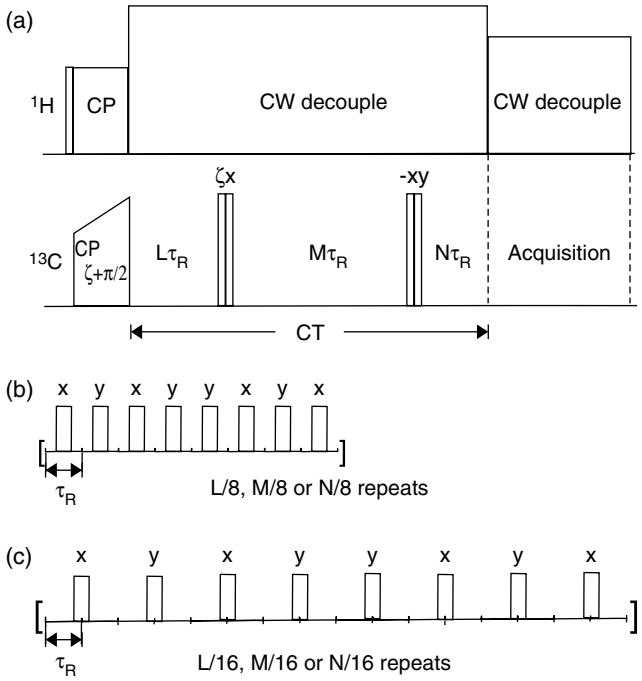

Figure 1. (a) The displayed fpCTDQBU pulse sequence included: (1) cross-polarization (*CP*) from ^{1}H nuclei to ^{13}C nuclei, (2) a constant-time (*CT*) period of $(L + M + N)\tau_R$ duration where *L*, *M*, and *N* were integral multiples of 8 or 16, and τ_R was the duration of a single rotor period and (3) an acquisition period during which ^{13}C NMR signals were detected. Continuous wave ^{1}H decoupling was applied during the *CT* and the acquisition periods. A pair of back-to-back ^{13}C $\pi/2$ pulses separated the $L\tau_R$ and the $M\tau_R$ periods and another pair separated the $M\tau_R$ and the $N\tau_R$ periods. Variants of the pulse sequence during the *CT* period included: (b) the 'one-π-per-τ_R' version with one ^{13}C π pulse per rotor period and (c) the 'one-π-per-$2\tau_R$' version with one ^{13}C π pulse per two rotor periods. The ^{13}C *CP* rf phase was $\zeta + \pi/2$ and the phase of each ^{13}C $\pi/2$ and π pulse is noted above the pulse. For $\zeta = y$ or $-y$, ^{13}C–^{13}C dipolar evolution was refocused over a period of $2L\tau_R$ duration and S_0 data were obtained and for $\zeta = x$ or $-x$, ^{13}C–^{13}C dipolar evolution was not refocused during this period and S_1 data were obtained. The duration of the ^{13}C–^{13}C dipolar recoupling or dephasing period was therefore $\tau = 2L\tau_R$, and data with increasing τ were obtained by incrementing *L* and decrementing *N* while keeping constant $M = L + N$ and constant $(L + M + N)$.

DOI: 10.1002/mrc

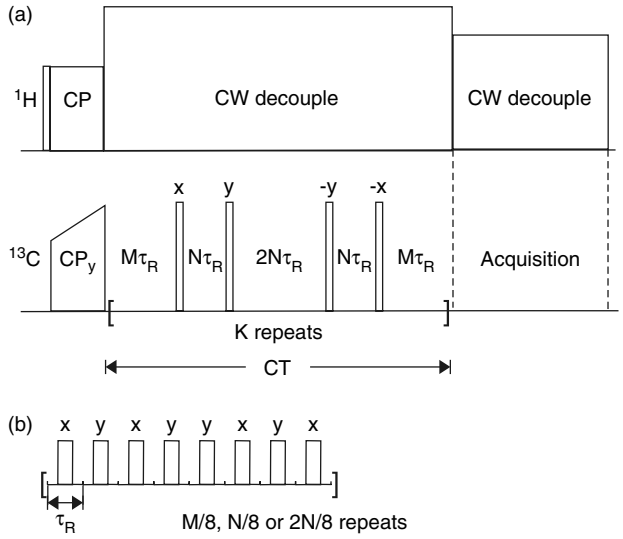

Figure 2. (a) The displayed fpRFDR-CT pulse sequence included cross-polarization (*CP*) from ^{1}H nuclei to ^{13}C nuclei, a constant-time (*CT*) period, and an acquisition period during which ^{13}C NMR signals were detected. Continuous wave ^{1}H decoupling was applied during the *CT* and the acquisition periods. The *CT* period contained *K* cycles of $(2M + 4N)\tau_R$ duration where *K* was an integer, *M* and *N* were integral multiples of 8, and τ_R was the duration of a single rotor period. Each $(2M + 4N)\tau_R$ cycle contained intervals separated by ^{13}C $\pi/2$ pulses and panel and (b) displays the series of ^{13}C π pulses in each of these intervals. The ^{13}C *CP* rf phase was *y* and the phase of each ^{13}C $\pi/2$ and π pulse is noted above the pulse. Each $(2M + 4N)\tau_R$ cycle could be understood to have a central $6N\tau_R$ WAHUHA period during which the ^{13}C–^{13}C dipolar evolution was refocused. For $M = N$, the *CT* period can be considered as a series of WAHUHA periods and S_0 data were obtained with no dipolar coupling period. For $M > N$, ^{13}C–^{13}C dipolar evolution was not completely refocused and S_1 data were obtained. The total duration of the ^{13}C–^{13}C dipolar recoupling or dephasing period was $\tau = 2K \times (M - N)\tau_R$ and data with increasing τ were obtained by incrementing *M* and decrementing *N* while keeping $(M + 2N)$ and *K* constant.

commute with one another and $H_{xx} + H_{yy} + H_{zz} = 0$ where $H_{xx} = 3I_{x1}I_{x2} - \boldsymbol{I}_1.\boldsymbol{I}_2$ yields:

$$U(\tau) = e^{(i\pi/2)I_x}e^{(-i\pi/2)I_y}e^{(DL\tau_R)H_{xx}} \quad (5)$$

The initial density operator $\rho(0)$ immediately after *CP* is proportional to $I_x = I_{x1} + I_{x2}$ so that:

$$\begin{aligned}\rho(\tau) = U(\tau)\rho(0)U^{-1}(\tau) &\propto e^{(i\pi/2)I_x}e^{(-i\pi/2)I_y}e^{(DL\tau_R)H_{xx}}I_x \\ &\times e^{(-DL\tau_R)H_{xx}}e^{(i\pi/2)I_y}e^{(-i\pi/2)I_x} \\ &= e^{(i\pi/2)I_x}e^{(-i\pi/2)I_y}I_x e^{(i\pi/2)I_y}e^{(-i\pi/2)I_x} = -I_y \end{aligned} \quad (6)$$

Within the context of average Hamiltonian theory, the ^{13}C evolution during the $2L\tau_R$ period for $\zeta = -y$ is a 90° rotation of the ^{13}C magnetization in the transverse plane. The evolution during the subsequent $2N\tau_R$ period is similarly derived and yields $\rho(CT) = -I_y$. For $\zeta = y$, $\rho(CT) = -I_y$ while for $\zeta = x$ and $-x$, there is net loss of observable magnetization during the $2L\tau_R$ period because of dipolar evolution.

fpRFDR-CT spectroscopy

Figure 2(a) displays the fpRFDR-CT sequence that had the form $CP_y - [(fpRFDR)_M - \pi/2_x - (fpRFDR)_N - \pi/2_y - (fpRFDR)_{2N} - \pi/2_{-y} - (fpRFDR)_N - \pi/2_{-x} - (fpRFDR)_M]_K$ $-$ *acquisition* where *M* and *N* were integral multiples of 8, $(fpRFDR)_M$ and $(fpRFDR)_N$ had durations $M\tau_R$ and $N\tau_R$, and *K* was an integer. Transverse ^{13}C magnetization was generated during the *CP* period, evolved during the *fpRFDR* periods, and was detected during the acquisition period. During the *fpRFDR* periods, ^{13}C chemical shift evolution was refocused by the rotor-synchronized ^{13}C π pulses. For $M = N = M_0$, S_0 data were obtained because each cycle of $(fpRFDR)_M - \pi/2_x - (fpRFDR)_N - \pi/2_y - (fpRFDR)_{2N} - \pi/2_{-y} - (fpRFDR)_N - \pi/2_{-x} - (fpRFDR)_M$ can be considered as a series of WAHUHA periods with refocusing of the ^{13}C–^{13}C dipolar evolution. For $M > N$, ^{13}C–^{13}C dipolar evolution was not refocused during the initial $(fpRFDR)_{M-N}$ and final $(fpRFDR)_{M-N}$ periods of each cycle and S_1 data were obtained. Data with increasing dipolar coupling time τ were obtained by incrementing *M* by 'ΔM' which was an integral multiple of 16 and decrementing *N* by $\Delta M/2$ so that $\tau = 2K \times (M - N)\tau_R = 3K\Delta M\tau_R$ and the total $CT = 2K \times (M + 2N)\tau_R = 6KM_0\tau_R$. The full phase cycle included the $(CP_y \ldots \pi/2_x \ldots \pi/2_y \ldots \pi/2_{-y} \ldots \pi/2_{-x})$ ^{13}C phases displayed in Fig. 2(a) as well as the $(CP_{-x} \ldots \pi/2_y \ldots \pi/2_{-x} \ldots \pi/2_x \ldots \pi/2_{-y})$, $(CP_{-y} \ldots \pi/2_{-x} \ldots \pi/2_{-y} \ldots \pi/2_y \ldots \pi/2_x)$, and $(CP_x \ldots \pi/2_{-y} \ldots \pi/2_x \ldots \pi/2_{-x} \ldots \pi/2_y)$ ^{13}C phases with *y*, $-x$, $-y$, and *x* receiver phases, respectively.

Transverse ^{13}C relaxation (T_2) measurements

For the fpRFDR-CT experiment, the ^{13}C magnetization was longitudinal during the period between the first and second $\pi/2$ pulses and the period between the third and fourth $\pi/2$ pulses. For the dephasing period $\tau = 3K\Delta M\tau_R$, the total ^{13}C transverse relaxation period $\tau_T = 2K \times (M + N)\tau_R = K \times (4M_0 + \Delta M)\tau_R$. Quantitative interpretation of the fpRFDR-CT data therefore required consideration of ^{13}C transverse relaxation and ^{13}C T_2 times were measured with a Carr–Purcell multiple echo sequence containing $CP_x - [Q\tau_R - \pi_y - 2Q\tau_R - \pi_{-y} - Q\tau_R - \text{detect}]_P$ where *Q* was an even integer, *P* was an integer, and a data set consisted of echo signals with different values of *P*.[57] For all samples, the echo intensities $E(t)$ fitted well to a single exponential decay $E(t) = E(0)\,exp(-t/T_2)$ where $t = 4QP\tau_R$. The uncertainties in the fitted T_2 values were $< \pm 8\%$. Experimental parameters for the Carr–Purcell sequence included 10 kHz MAS frequency, ~65 kHz ^{13}C π pulses, and ~95 kHz CW ^{1}H decoupling.

Experimental data analysis

For each pair of S_0 and S_1 fpCTDQBU spectra with a particular dephasing time τ, integrated signal intensities in the isotropic carbonyl regions were denoted as S_0 and S_1, respectively. A single experimental uncertainty σ was calculated as the root-mean-squared deviation of integrated intensities in 24 regions of the S_0 and S_1 spectra which contained noise rather than signal. The integrated intensities were incorporated into the normalized dephasing parameter:

$$\left(\frac{\Delta S}{S_0}\right)^{\exp} = \frac{S_0 - S_1}{S_0} = 1 - \frac{S_1}{S_0} \quad (7)$$

DOI: 10.1002/mrc

The ΔS^{exp} was the double-quantum filtered signal and the factor $1/S_0{}^{exp}$ compensated for T_2 decay for comparison with simulations which did not consider T_2 decay. The uncertainty in $(\Delta S/S_0)^{exp}$ was calculated as follows[58]:

$$\sigma^{exp} = \frac{\sigma}{S_0}\sqrt{1+\frac{S_1{}^2}{S_0{}^2}} = \frac{\sigma\, S_1}{S_0}\sqrt{\frac{1}{S_1{}^2}+\frac{1}{S_0{}^2}} \quad (8)$$

The fpRFDR-CT data were similarly analyzed except that for each value of τ, there was only one spectrum. The $\tau = 0$ spectrum with no dipolar coupling period was denoted as S_0 and the other spectra with variable dipolar coupling periods were denoted as S_1. In addition, separate σ_{S_0} and σ_{S_1} were calculated as the root-mean-squared deviations of integrated intensities in 12 regions of the S_0 and S_1 spectra without signal. The normalized dephasing parameter for the fpRFDR-CT data was $(S_1/S_0)^{exp}$ and the uncertainty in $(S_1/S_0)^{exp}$ was calculated:

$$\sigma^{exp} = \sqrt{\frac{\sigma_{S_1}{}^2}{S_0{}^2}+\frac{S_1{}^2\sigma_{S_0}{}^2}{S_0{}^4}} = \frac{S_1}{S_0}\sqrt{\frac{\sigma_{S_1}{}^2}{S_1{}^2}+\frac{\sigma_{S_0}{}^2}{S_0{}^2}} \quad (9)$$

For $\tau = 0$, $S_1/S_0 = 1$ and $\sigma^{exp} = \sqrt{2}\sigma_{S_0}/S_0$.

One goal of this study was quantitative comparison between the $(\Delta S/S_0)^{exp}$ or $(S_1/S_0)^{exp}$ and simulations done for two or three ^{13}C with different internuclear distances. However, the experimental samples contained natural abundance ^{13}C close to the labeled ^{13}C and the experimental ^{13}C labeling was ~99%. Values of $(\Delta S/S_0)^{cor}$ and $(S_1/S_0)^{cor}$ were calculated from $(\Delta S/S_0)^{exp}$ and $(S_1/S_0)^{exp}$ to compensate for these effects and followed the correction methods detailed in previous work.[22] As one example, the following approximations were used to calculate $(\Delta S/S_0)^{cor}$ for D-GFF.

First, there were approximations relevant to calculation of $S_0{}^{cor}$ and $S_1{}^{cor}$:

1. ^{13}CO signals from Gly-1, Phe-2, and Phe-3 were completely resolved.
2. There was 99% labeling of Gly-1 ^{13}CO and Phe-3 ^{13}CO.

There were also approximations only relevant to calculation of $S_1{}^{cor}$:

3. Intermolecular ^{13}C–^{13}C dipolar coupling was not considered. For Gly-1 ^{13}CO, the closest intermolecular carbon nucleus was >4 Å away.
4. $S_1 = S_0$ for a molecule with a labeled Gly-1 ^{13}CO and a Phe-3 ^{12}CO.
5. S_1 values for a molecule with a labeled Gly-1 ^{13}CO and nearby natural abundance ^{13}C were set with the following criteria: (5a) $S_1 = 0$ when $\tau \leq 32$ ms and the labeled Gly-1 ^{13}CO/natural abundance ^{13}C nuclei were separated by one or two bonds. (5b) $S_1 = 0$ when $\tau > 32$ ms and the labeled Gly-1 ^{13}CO/natural abundance ^{13}C nuclei were separated by one, two, or three bonds. (5c) S_1 was not affected by the natural abundance ^{13}C if neither criterion 5a nor 5b was satisfied. The criteria were based on the ~1.5, ~2.5 and ~3.8 Å distances for one-, two- and three-bond ^{13}C–^{13}C separations, respectively, and the consequent 2200 , 500 , and 140 Hz dipolar couplings.
6. $S_1 = S_0$ for a natural abundance Gly-1 ^{13}CO in an unlabeled GFF molecule.

The expression of $(\Delta S/S_0)^{cor}$ for D-GFF was:

$$\left(\frac{\Delta S}{S_0}\right)^{cor} = \frac{1-U_{C1}+n\,A_C}{1-U_{C1}-U_{C2}-m\,A_C}\left(\frac{\Delta S}{S_0}\right)^{exp} - \frac{m\,A_C}{1-U_{C1}-U_{C2}-m\,A_C} \quad (10)$$

where $U_{C1} = 0.01$ and $U_{C2} = 0.01$ were the fractions of Gly-1 and Phe-3 ^{12}CO sites in D-GFF, respectively; $A_C = 0.011$ was the fractional ^{13}C natural abundance; $n = 49$ was the ratio of unlabeled GFF to D-GFF molecules in the crystal; and m was the number of unlabeled carbon nuclei which satisfy either criterion 5a or 5b. Incorporation of the previously noted parameter values for $\tau \leq 32$ ms and $m = 2$ yielded:

$$\left(\frac{\Delta S}{S_0}\right)^{cor} = 1.596\left(\frac{\Delta S}{S_0}\right)^{exp} - 0.023 \quad (11)$$

and for $\tau > 32$ ms and $m = 4$ yielded:

$$\left(\frac{\Delta S}{S_0}\right)^{cor} = 1.634\left(\frac{\Delta S}{S_0}\right)^{exp} - 0.047 \quad (12)$$

The expressions for $(\Delta S/S_0)^{cor}$ of D-NAL were determined in a manner similar to those of D-GFF.

The $(\Delta S/S_0)^{cor}$ of the membrane-associated HFPs were analyzed in the context of two structural populations. For one population with fraction h, there was a detectable dipolar coupling (d) between the labeled ^{13}COs and for the other population with fraction $1-h$, $d = 0$. The resulting $(\Delta S/S_0)^{cor}$ had a general form:

$$\left(\frac{\Delta S}{S_0}\right)^{cor} = \frac{1-U_C+n\,A_C}{h(1-U_C-m\,A_C)}\left(\frac{\Delta S}{S_0}\right)^{exp} - \frac{m\,A_C}{h(1-U_C-m\,A_C)} \quad (13)$$

The fpRFDR-CT $(S_1/S_0)^{cor}$ expressions were similarly derived and yielded a general expression for D-GFF and D-NAL:

$$\left(\frac{S_1}{S_0}\right)^{cor} = \frac{1-U_{C1}+n\,A_C}{1-U_{C1}-U_{C2}-m\,A_C}\left(\frac{S_1}{S_0}\right)^{exp} - \frac{n\,A_C+U_{C2}}{1-U_{C1}-U_{C2}-m\,A_C} \quad (14)$$

The $(\Delta S/S_0)^{cor}$ or the $(S_1/S_0)^{cor}$ expressions had the general form $a \times (\Delta S/S_0)^{exp} - b$ or $a \times (S_1/S_0)^{exp} - b$, respectively, where a and b were positive numbers. The σ^{cor} associated with $(\Delta S/S_0)^{cor}$ and $(S_1/S_0)^{cor}$ were therefore $a \times \sigma^{exp}$. The overall data analysis included the goodness-of-fit metric χ^2 that had $(\sigma^{cor})^{-2}$ dependence. Although the h in the HFP analysis was a fitting parameter, the HFP σ^{cor} were calculated with $h = 1$ and the variations of χ^2 with h were therefore independent of σ^{cor}.

fpCTDQBU and fpRFDR-CT simulations

$(\Delta S/S_0)^{sim}$ and $(S_1/S_0)^{sim}$ were calculated as a function of the labeled ^{13}CO–^{13}CO dipolar coupling d and dephasing time τ. The D-NAL and D-GFF simulations considered the two ^{13}CO sites in a single molecule while the HFP simulations considered three ^{13}CO sites with each site on a different HFP

DOI: 10.1002/mrc

strand. Three HFP strands were used both because there were three strands in HFPtr and because simulations with more than three spins required significantly more computer time. In a previous study, similar ^{13}CO–^{13}CO distances were obtained when fitting HFP experimental data with simulations based on two ^{13}CO spins or three ^{13}CO spins.[22] The number of structures considered in the HFP simulations was reduced to a tractable number by choosing an in-register parallel strand geometry with a single variable distance r and dipolar coupling d between the ^{13}CO in the central strand and the ^{13}COs in each of the two outside strands. The simulations also incorporated the weak dipolar coupling between the ^{13}COs in the outside strands.

The simulations were done with the simulation program for solid-state NMR spectroscopy (SIMPSON) program and incorporated the ^{13}C part of the fpCTDQBU or the fpRFDR-CT sequences including the MAS frequency and the ^{13}C rf fields, pulse lengths, timing, and phases but did not incorporate ^{1}H.[59] Additional input parameters included the ^{13}CO CSA principal values, the Euler angles that related the CSA principal axis system to a fixed crystal axis system, and the Euler angles that related the ^{13}CO–^{13}CO internuclear vector to the crystal axis system. The fpCTDQBU and fpRFDR-CT simulations were not significantly sensitive to these additional parameters but some effort was still made to choose reasonable parameter values.[22]

The ^{13}CO CSA principal values of NAL and GFF were determined by fitting experimental centerband and spinning sideband intensities with the Herzfeld–Berger method.[60] In ppm units, the (δ_{11}, δ_{22}, δ_{33}) principal values of the carbonyl and carboxyl sites of D-NAL were (246, 201, 87) and (258, 172, 109), respectively, and the principal values of the Gly-1 and Phe-3 sites of D-GFF were (254, 168, 90) and (243, 193, 106), respectively. For the membrane-associated HFP samples, the ^{13}CO CSA principal values were determined from experimental isotropic chemical shifts and literature anisotropy values and were (242, 191, 85), (240, 193, 85) and (242, 195, 87) for HFPmn-F8, HFPtr-A6, and HFPtr-A15, respectively.[61,62]

The Euler angles that related the ^{13}CO CSA principal axis system to the crystal axis system can be considered in terms of the relative orientation of the principal axis system and the ^{13}CO chemical bonds and the orientation of the molecule relative to the crystal axes. For the NAL, HFP, and GFF Gly-1 ^{13}COs, literature data were used to set the ^{13}CO CSA δ_{33} axis perpendicular to the peptide plane and the δ_{22} axis at an angle of 130° from the C–N bond.[62] For GFF, the Phe-3 carboxyl group was negatively charged and the ^{13}CO CSA δ_{33} axis was set perpendicular to the OCO plane and the δ_{11} axis was set along the bisector of the OCO angle.[63,64]

In the labeled ^{13}CO regions of peptides, the local structure defines the relative orientation of the ^{13}C–^{13}C internuclear vector with respect to the ^{13}CO chemical bonds and CSA principal axis system. The chemical shifts of the membrane-associated HFPs were all consistent with β-strand conformation and their molecular orientation in the crystal frame was set using atomic coordinates derived from a parallel β-strand region of a protein with a high-resolution crystal structure. The name of the protein is cutinase, its Protein Data Bank (PDB) file name is 1cex, and coordinates from the residues Ile-34 to Ala-38, Val-68 to Gly-72, and Thr-113 to Gly-118 were used.[65] The atomic coordinates and ^{13}CO CSA principal axis directions were inputs to calculate the Euler angles for the ^{13}CO principal axis system and the ^{13}CO–^{13}CO internuclear vectors in the crystal frame.

Some SIMPSON simulations were done on a PC with a WINDOWS operating system and a 1.7 GHz processor while other simulations were performed on a LINUX cluster using two 1.8 GHz processors.

As noted earlier in the paper, the fpRFDR-CT dephasing period $\tau = 3K\Delta M\tau_R$ and the transverse relaxation period $\tau_T = K(4M_0 + \Delta M)\tau_R$, and the effect of differential transverse relaxation was empirically incorporated into the simulation results with multiplication of $(S_1/S_0)^{sim}$ by $exp(-\tau/3T_2)$.

Determination of best-fit internuclear distances

For the fpCTDQBU experiments, comparison was made between $(\Delta S/S_0)^{cor}$ and $(\Delta S/S_0)^{sim}$ calculated as a function of d and the best-fit d was determined from χ^2 fitting:

$$\chi^2 = \chi^2(d) = \sum_{j=1}^{N} \frac{\left(\left(\frac{\Delta S}{S_0}\right)_j^{cor} - \left(\frac{\Delta S}{S_0}(d)\right)_j^{sim}\right)^2}{\left(\sigma_j^{cor}\right)^2} \qquad (15)$$

where the j subscript refers to a particular τ and N was the total number of τ.

For the fpRFDR-CT experiments, analogous analysis was done using $(S_1/S_0)^{cor}$ and $(S_1/S_0)^{sim}$ in the χ^2 expression.

RESULTS

fpCTDQBU spectra

Figure 3 displays, for example, ^{13}C fpCTDQBU spectra of different samples. For each panel, peak shifts in ppm and assignments were: **a**, 180.1, carboxyl; and 178.4, amide COs of D-NAL; **b**, 180.3, Phe-3; 176.7, Phe-2; and 170.8, Gly-1 COs of D-GFF; **c**, 172.6, CO of membrane-associated HFPmn-F8; and **d**, 174.9, CO of membrane-associated HFPtr-A15. The ^{13}CO signals of the membrane-HFP samples had ~75 and ~25% respective contributions from labeled and natural abundance sites. The peak shift of the HFPmn-F8 spectra agreed better with the database distribution of β-strand ^{13}CO shifts for Phe (174.3 ± 1.6 ppm) than with the distribution of helical shifts (177.1 ± 1.4 ppm).[66] A β-strand conformation at this site was also supported by previous torsion angle measurements.[35] The peak shift of the HFPtr-A6 spectra was 173.7 with ~3 ppm peak width and line shape similar to those of the HFPmn-F8 spectra. The HFPtr-A6 shift was also more consistent with the database distribution of β-strand shifts for Ala (176.1 ± 1.5 ppm) than with the distribution of helical shifts (179.4 ± 1.3 ppm).[66] The peak shift of the HFPtr-A15 spectra was also consistent with β-strand conformation but the peak was broader than the other two HFP samples which may indicate greater conformational heterogeneity near Ala-15.

In Fig. 3(a), $(\Delta S/S_0)^{exp} > 0.9$ for the D-NAL spectra which was a reasonable result because $d = 270$ Hz and $d\tau = 3.6$. In Fig. 3(b), $(\Delta S/S_0)^{exp} \approx 0.55$ for the D-GFF spectra with $d = 49$ Hz and $d\tau = 1.4$. The Gly-1 and Phe-3 signals included ~35% contribution from natural abundance

DOI: 10.1002/mrc

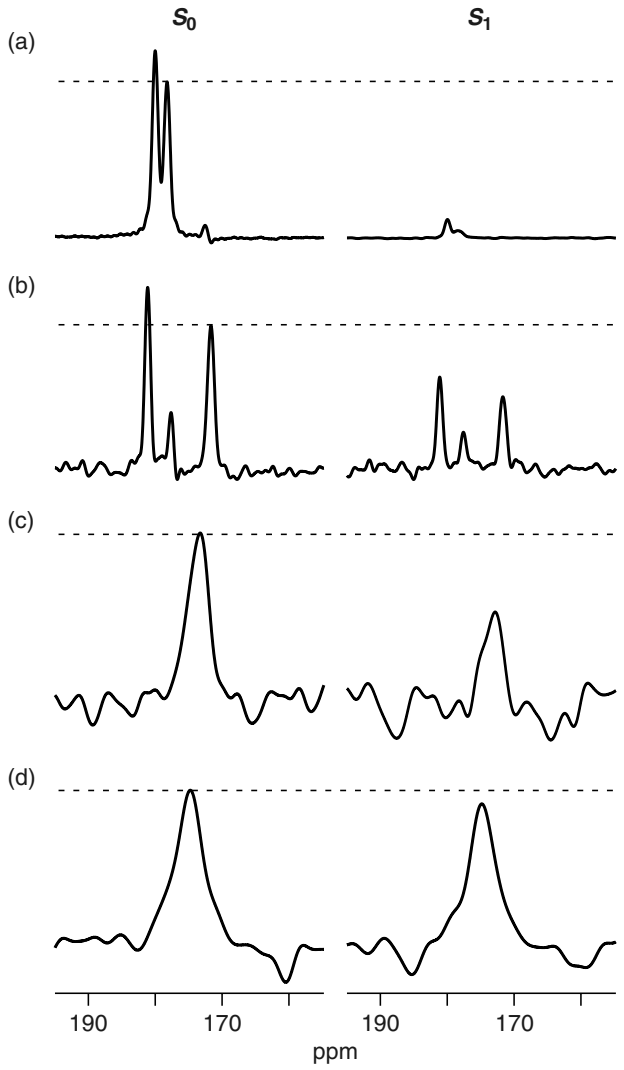

Figure 3. ^{13}C one-π-per-τ_R fpCTDQBU spectra of: (a) D-NAL with $\tau = 13.33$ ms (b) D-GFF with $\tau = 28.00$ ms (c) membrane-associated HFPmn-F8 with $\tau = 29.33$ ms and (d) membrane-associated HFPtr-A15 with $\tau = 30.67$ ms. The MAS frequency was 12 000 Hz and (a) $CT = 20.0$ ms (b) $CT = 41.33$ ms or (c, d) $CT = 64.0$ ms. For each lettered pair of spectra, the S_0 spectrum is on the left and represented the sum of $\zeta = y$ and $\zeta = -y$ data and the S_1 spectrum is on the right and represented the sum of $\zeta = x$ and $\zeta = -x$ data. Dotted lines are drawn at the peak labeled amide carbonyl S_0 intensities. Each spectrum in panel (a), (b), (c), or (d) respectively represented the sum of 64, 4000, 10 000, or 10 000 scans and was respectively processed with 75, 75, 200, or 300 Hz Gaussian line broadening. Processing also included dc offset correction and polynomial baseline correction.

^{13}COs and the natural abundance sites had $(\Delta S/S_0) \approx 0$. The membrane-associated HFP spectra of Fig. 3(c–d) were obtained with $\tau \approx 30$ ms and offered an interesting contrast with $(\Delta S/S_0)^{exp} \approx 0.5$ for HFPmn-F8 and <0.1 for HFPtr-A15. The signals had ~25% contribution from natural abundance sites and comparison with the GFF spectra qualitatively suggested labeled ^{13}CO–^{13}CO distances close to 5 Å in the HFPmn-F8 sample and much greater than 5 Å in the HFPtr-A15 sample.

Comparison between fpCTDQBU and fpRFDR-CT experiments

For the version of the fpCTDQBU method in this study, there was a S_0 and a S_1 acquisition for each dephasing period τ. For the fpRFDR-CT method, there was only one S_0 acquisition per data set and consequent higher sensitivity because for a fixed total time for data acquisition, more time was available for signal averaging of S_1 spectra. On the other hand, data analysis for this version of fpRFDR-CT had greater complexity because the contribution of transverse relaxation was τ-dependent.

Figure 4 displays an initial comparison of the two experiments using the D-GFF sample for which the labeled ^{13}CO–^{13}CO distance was comparable to the structurally interesting distances in the HFP samples. The $(\Delta S/S_0)^{cor}$ derived from the fpCTDQBU experiment were fitted to $(\Delta S/S_0)^{sim}$ calculated as a function of d and Fig. 4(a) displays $(\Delta S/S_0)^{cor}$ and best-fit $(\Delta S/S_0)^{sim}$ plotted as functions of τ. The best-fit value of d was 49.4 ± 1.2 Hz with corresponding $r = 5.39 \pm 0.05$ Å which agreed with $r = 5.40$ Å in the crystal structure.[52] As displayed in Fig. 4(b), a similar analysis was done for the $(S_1/S_0)^{cor}$ calculated from the fpRFDR-CT data and $(S_1/S_0)^{sim}$ which incorporated the experimentally-derived $T_2 = 54$ ms. The T_2 correction had the functional form $exp(-\tau/162\text{ ms})$ and had a minor effect on the data analysis because the decay constant for $(S_1/S_0)^{cor}$ was ~30 ms. The best-fit $d = 59 \pm 3$ Hz corresponded to $r = 5.07 \pm 0.09$ Å. Comparison of the fpCTDQBU and fpRFDR-CT results for microcrystalline GFF showed that the fpCTDQBU method was more quantitative and the fpRFDR-CT method yielded higher signal-to-noise which agreed with expectations for the two approaches.

Figure 5 displays plots of fpCTDQBU $(\Delta S/S_0)^{cor}$ *versus* τ and fpRFDR-CT $(S_1/S_0)^{cor}$ *versus* τ for the membrane-associated HFP samples. Figure 5(a) shows qualitative differences between the fpCTDQBU data of the three samples with the largest $(\Delta S/S_0)^{cor}$ buildup for the HFPmn-F8 sample and $(\Delta S/S_0)^{cor} \approx 0$ for the HFPtr-A15 sample when $\tau < 35$ ms. There were much less pronounced differences among the fpRFDR-CT data which might be understood from the measured $T_2 \approx 15$ ms for these samples and the expected $exp(-\tau/45\text{ ms})$ decay that would be d-independent. The shorter T_2 contrasts with the longer T_2 of GFF as well as the $T_2 \sim 50$ ms reported for ^{13}Cs in fibrilized amyloid fibrils.[21] The Fig. 5 data suggested that ^{13}CO–^{13}CO distances in the membrane-associated HFP samples would be more straightforwardly derived from the fpCTDQBU experiment and this method was the focus of our subsequent study.

Optimization of fpCTDQBU parameters

It was shown in a previous study that use of longer rather than shorter ^{13}C π pulses in the fpCTDQBU experiment resulted in faster buildup of $(\Delta S/S_0)^{exp}$ with τ.[22] Faster buildup allowed use of smaller CT values with the concomitant effect of increasing S_0 and S_1 signal intensities. However, for the moderate 12 kHz MAS frequency of our experiments, longer π pulses also reduced chemical shift refocusing with the effect of decreasing S_0 and S_1 signal

DOI: 10.1002/mrc

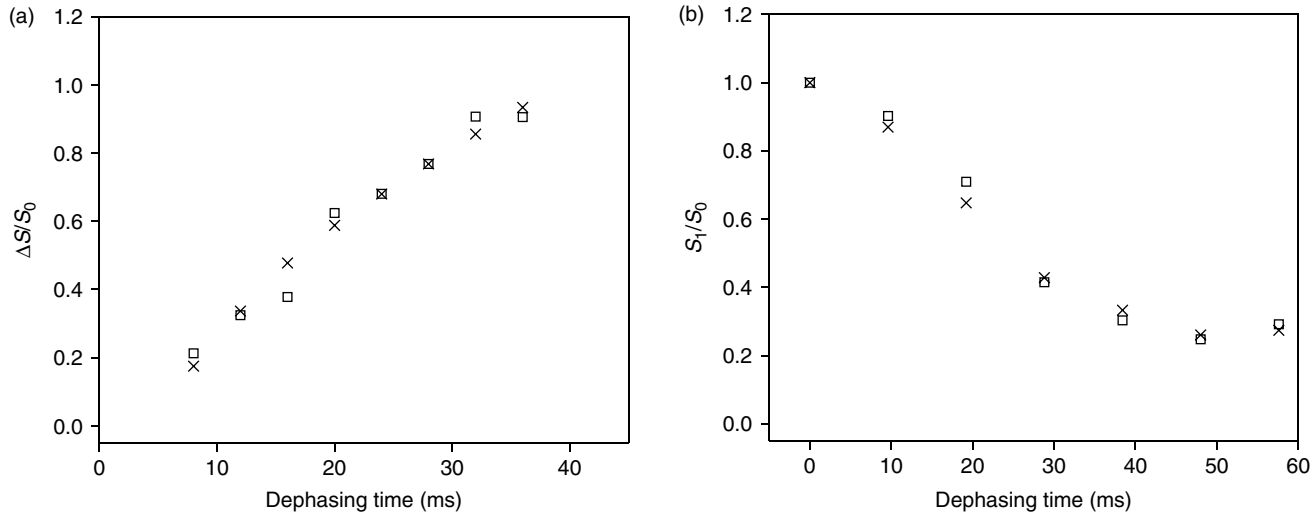

Figure 4. (a) Plot of D-GFF fpCTDQBU $(\Delta S/S_0)^{cor}$ (squares) and $(\Delta S/S_0)^{sim}$ (crosses) *versus* dephasing time. Acquisition parameters included one-π-per-τ_R, MAS frequency = 12 000 Hz, 20.5 kHz ^{13}C π pulses, and CT = 41.33 ms. Each $(\Delta S/S_0)^{cor}$ was calculated from a $(\Delta S/S_0)^{exp}$ determined with S_0 and S_1 spectra that each represented the sum of 4000 scans. The integration regions were 1 ppm and were centered at 170.8 ppm which was the peak shift of the Gly-1 ^{13}CO in the S_0 spectra. The σ^{cor} were ~0.05. The displayed $(\Delta S/S_0)^{sim}$ were calculated with the best-fit $d = 49.4 \pm 1.2$ Hz and corresponding $r = 5.39 \pm 0.05$ Å for the Gly-1/Phe−3 ^{13}CO labeled pair. The $\chi^2 = 8.4$ for this best-fit value. (b) Plot of D-GFF fpRFDR-CT $(S_1/S_0)^{cor}$ (squares) and $(S_1/S_0)^{sim}$ (crosses) *versus* dephasing time. Acquisition parameters included MAS frequency = 10 000 Hz, 15.2 kHz ^{13}C π pulses, and CT = 67.2 ms. Each $(S_1/S_0)^{cor}$ was calculated from a $(S_1/S_0)^{exp}$ determined with S_0 and S_1 spectra that each represented the sum of 2048 scans. The integration regions were 1 ppm and were centered at the Gly-1 ^{13}CO peak (170.8 ppm) and the σ^{cor} were ~0.04. The displayed $(S_1/S_0)^{sim}$ were calculated with the best-fit $d = 59.0 \pm 3.0$ Hz and corresponding $r = 5.07 \pm 0.09$ Å. The $\chi^2 = 4.0$ for this best-fit value.

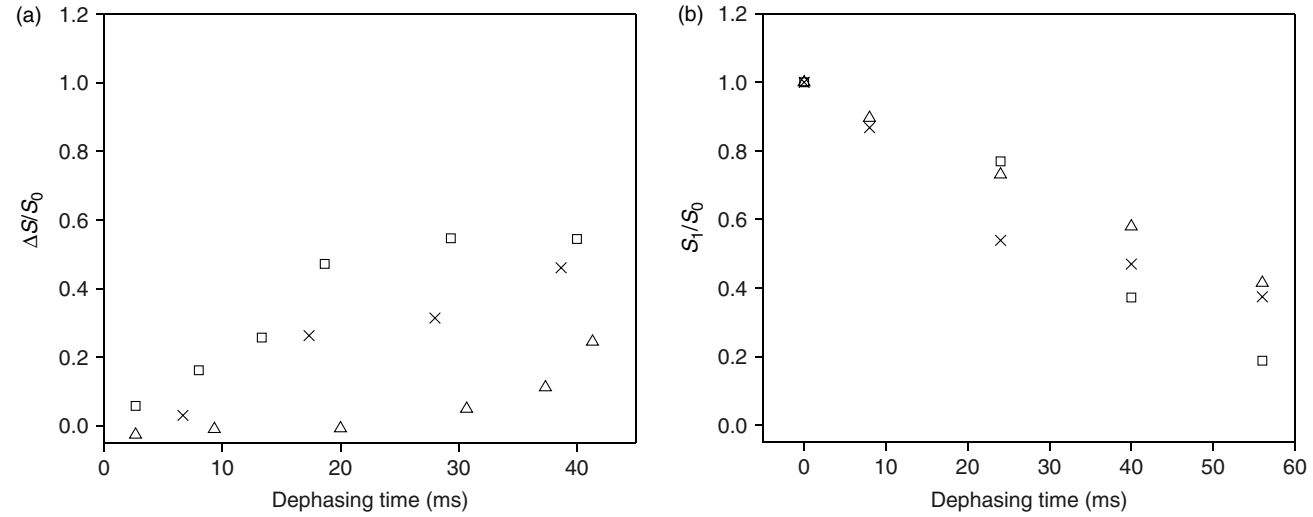

Figure 5. (a) Plot of fpCTDQBU $(\Delta S/S_0)^{cor}$ *versus* dephasing time for membrane-associated HFPmn-F8 (squares), HFPtr-A6 (crosses) and HFPtr-A15 (triangles). Acquisition parameters included one-π-per-τ_R, MAS frequency = 12000 Hz, 20.5 kHz ^{13}C π pulses, and CT = 64.00 ms for HFPmn-F8 and HFPtr-A15 or CT = 41.33 ms for HFPtr-A6. Each $(\Delta S/S_0)^{cor}$ was calculated from a $(\Delta S/S_0)^{exp}$ determined with S_0 and S_1 spectra that each represented the sum of 10 000, ~40 000, and 10 000 scans for the HFPmn-F8, HFPtr-A6 and HFPtr-A15 samples, respectively. The integration regions were 2 ppm and the σ^{cor} were ~0.10, 0.06 and 0.09 for the HFPmn-F8, HFPtr-A6 and HFPtr-A15 samples, respectively. (b) Plot of fpRFDR-CT $(S_1/S_0)^{cor}$ *versus* dephasing time for membrane-associated HFPmn-F8 (squares), HFPtr-A6 (crosses), and HFPtr-A15 (triangles). Acquisition parameters included MAS frequency = 12000 Hz, 20.5 kHz ^{13}C π pulses, and CT = 64.00 ms. Each $(S_1/S_0)^{cor}$ was calculated from a $(S_1/S_0)^{exp}$ with S_0 and S_1 spectra that each represented the sum of 12 000, 33 000, and 21 000 scans for the HFPmn-F8, HFPtr-A6, and HFPtr-A15 samples, respectively. The integration regions were 2 ppm and the σ^{cor} were ~0.04, 0.10, and 0.08 for the HFPmn-F8, HFPtr-A6, and HFPtr-A15 samples, respectively. The $(\Delta S/S_0)^{cor}$ or $(S_1/S_0)^{cor}$ in each plot were calculated with $h = 1$, i.e. all labeled ^{13}CO experienced the same homonuclear dipolar coupling.

DOI: 10.1002/mrc

intensities. For samples with $d \approx 50$ Hz, an examination was made of $(\Delta S/S_0)$ buildup rates, corresponding reasonable CT values, and S_0 signal intensities as a function of π pulse length and it was found that there was a broad signal-to-noise maximum near 20 kHz π pulse field. Much of the optimization was done using SIMPSON simulations and these calculations were experimentally validated by spectra obtained with the D-GFF and D-NAL samples. Most of the subsequent fpCTDQBU experiments were done with 20.5 kHz π pulses.

The original implementations of the transverse RFDR or fpRFDR experiments for quantitative ^{13}C–^{13}C distance determination were done with the one-π-per-$2\tau_R$ version, *cf* Fig. 1(c).[17,22] The ratio of (total π pulse time)/τ for the one-π-per-τ_R version was two times larger than for the one-π-per-$2\tau_R$ version and the one-π-per-τ_R version might therefore exhibit a larger finite pulse effect and a more rapid buildup of $(\Delta S/S_0)$. This more rapid buildup was experimentally demonstrated for D-NAL and can be observed by visual comparison of the squares and crosses in Fig. 6(a). Use of shorter 35.0 kHz π pulses in the one-π-per-τ_R version decreased the buildup rate, *cf* up triangles in Fig. 6(a).

Because the ratio of (number of π pulses)/τ was two times larger for the one-π-per-τ_R version than for the one-π-per-$2\tau_R$ version, the one-π-per-τ_R version might exhibit reduced chemical shift refocusing and decreased S_0 and S_1 signals. This reduction was experimentally demonstrated for S_0 signals, *cf* squares *versus* crosses in Fig. 6(b). The S_0 signal could be partially recovered in the one-π-per-τ_R version by using 35.0 kHz π pulses, *cf* up triangles. A reasonable compromise was 20.5 kHz π pulses in the one-π-per-τ_R version with reduced CT, *cf* down triangles in Fig. 6(a), (b). Relative to longer CT data, the S_0 intensity was twice as large and a rapid buildup rate was retained for $(\Delta S/S_0)^{cor}$. These experimental parameters resulted in a duty factor $\tau_\pi/\tau_R = 0.3$ and fpRFDR rather than short-pulse RFDR was dominant in the average Hamiltonian.[19]

All of the S_0 data sets of Fig. 6(b) had inverted parabola shape with a maximum near $\tau/CT = 0.5$ and ~20% reduction in signal for $\tau/CT \approx 0.1$ or 0.9. The dipolar echo periods during the S_0 acquisition had durations 2τ and $CT - 2\tau$ and $S_0 \approx F(2\tau) \times F(CT - 2\tau)$ where $F(t)$ was the dipolar echo amplitude. The variation of S_0 with τ suggested that F may have both exponential and nonexponential decay components.

Figure 7 displays the effect of ^{13}C transmitter offset on $(\Delta S/S_0)$ of (a) D-NAL and (b) D-GFF. The offset parameter in ppm was defined as $\Delta = \delta_{transmitter} - \delta_{peak}$ where δ_{peak} was the average shift of the ^{13}CO labeled sites. For D-NAL in Fig. 7(a), there was little difference between $(\Delta S/S_0)^{cor}$ determined with $\Delta = -6.7$ or -16.7 ppm and similar invariance to offset was seen for $(\Delta S/S_0)^{sim}$. Invariant $(\Delta S/S_0)^{cor}$ and $(\Delta S/S_0)^{sim}$ were also observed for $\Delta = 12.7$ ppm (not shown). For the same Δ, there were systematic differences between $(\Delta S/S_0)^{cor}$ and $(\Delta S/S_0)^{sim}$ at large values of τ which are not currently understood. The best-fit d from $(\Delta S/S_0)^{cor}$ was also ~10% larger than the d calculated from the ^{13}CO–^{13}CO distance in the crystal structure. For D-GFF in Fig. 7(b), similar $(\Delta S/S_0)^{cor}$ were observed for $\Delta = 0$ or -12.0 ppm and yielded best-fit $d = 49.4$ or 44.6 Hz, respectively. The ^{13}CO–^{13}CO distance in the GFF crystal structure corresponded to $d = 49$ Hz.

Figure 8 displays the effect of variation of the ^{13}C π pulse nutation angle (θ) on $(\Delta S/S_0)$ of (a) D-NAL and (b) D-GFF. Each plot includes $(\Delta S/S_0)^{cor}$ and $(\Delta S/S_0)^{sim}$ calculated for $\theta = 180°$ and best-fit d. The plots also include $(\Delta S/S_0)^{sim}$ calculated with this d value but with different values of θ. For D-NAL, very similar $(\Delta S/S_0)^{sim}$ were obtained for $\theta = 170°$,

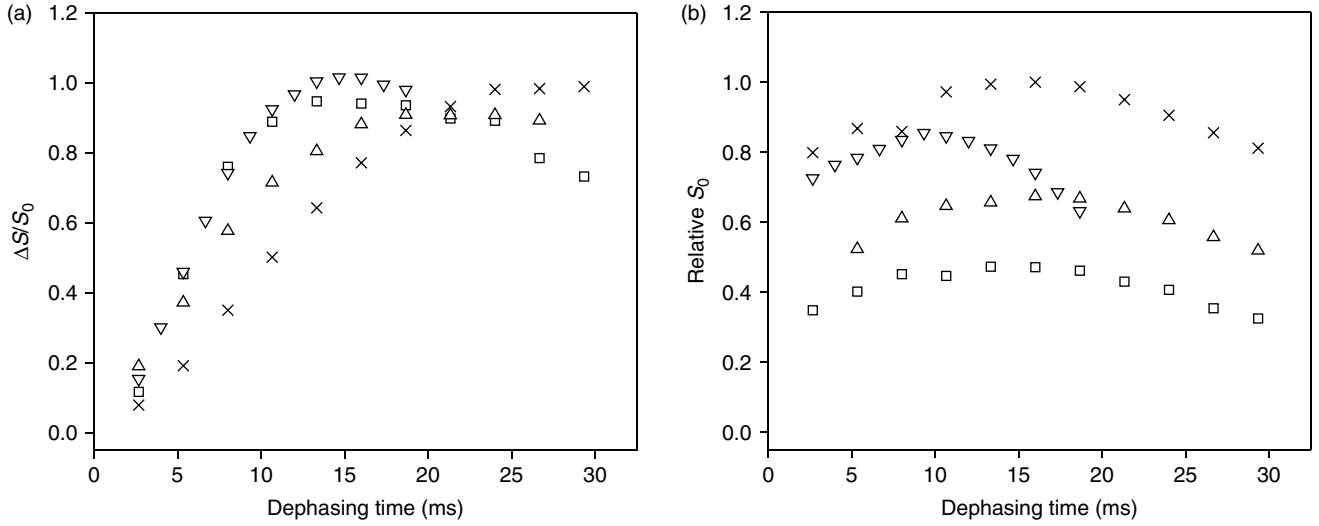

Figure 6. Plots of D-NAL fpCTDQBU (a) $(\Delta S/S_0)^{cor}$ and (b) S_0 *versus* dephasing time obtained with MAS frequency = 12 000 Hz. Each $(\Delta S/S_0)^{cor}$ was calculated from a $(\Delta S/S_0)^{exp}$ determined with S_0 and S_1 spectra that each represented the sum of 32 scans. The integration regions were 1 ppm and were centered at 178.3 ppm which was the peak carbonyl shift. The σ^{cor} were <0.006. For plot b, the cross (×) value of S_0 at $\tau = 16.0$ ms was set to 1.0 and the other S_0 were normalized relative to this value. The symbol legend: squares, one-π-per-τ_R, 20.5 kHz ^{13}C π pulses, $CT = 32.00$ ms; crosses, one-π-per-$2\tau_R$, 20.5 kHz ^{13}C π pulses, $CT = 32.00$ ms; up triangles, one-π-per-τ_R, 35.0 kHz ^{13}C π pulses, $CT = 32.00$ ms; down triangles, one-π-per-τ_R, 20.5 kHz ^{13}C π pulses, $CT = 20.00$ ms.

DOI: 10.1002/mrc

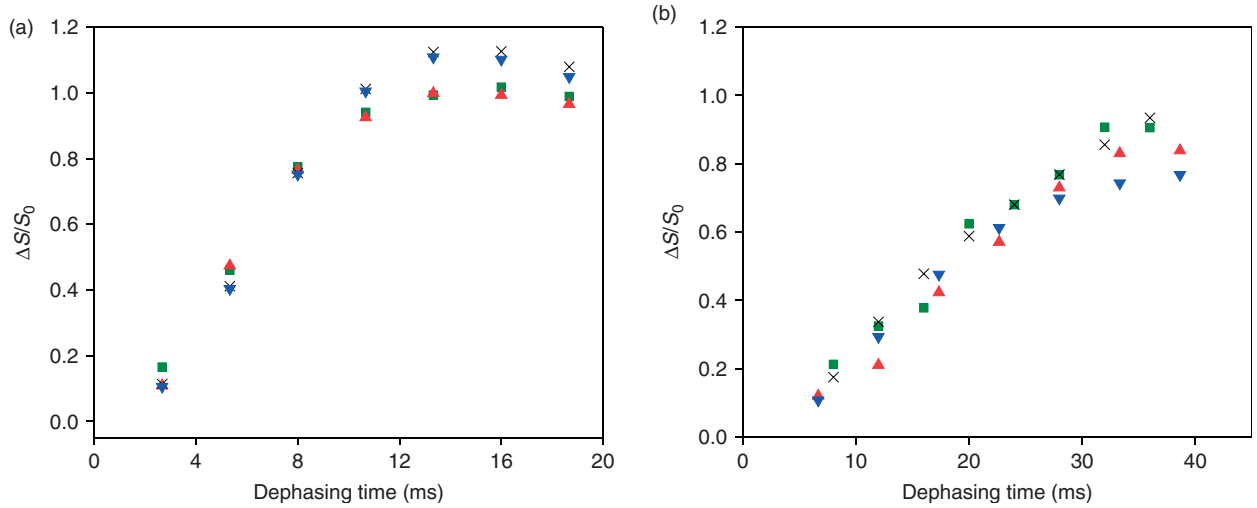

Figure 7. (a) D-NAL and (b) D-GFF plots of fpCTDQBU $(\Delta S/S_0)^{cor}$ and $(\Delta S/S_0)^{sim}$ *versus* dephasing time as a function of transmitter offset (Δ) calculated relative to the midpoint of the labeled carbonyl and carboxyl shifts. Acquisition parameters included one-π-per-τ_R, MAS frequency = 12 000, 20.5 kHz ^{13}C π pulses, and (a) $CT = 20.00$ ms or (b) $CT = 41.33$ ms. Each $(\Delta S/S_0)^{cor}$ was calculated from a $(\Delta S/S_0)^{exp}$ determined with S_0 and S_1 spectra that each represented the sum of (a) 32 or (b) 4000 scans. The integration regions were 1 ppm and were centered at (a) 178.3 or (b) 170.8 ppm which were the peak carbonyl shifts. The displayed $(\Delta S/S_0)^{sim}$ were calculated with the best-fit (a) $d = 296$ Hz or (b) $d = 49.4$ or 44.6 Hz for $\Delta = 0$ or -12.0 ppm, respectively. The symbol legend: green squares, $(\Delta S/S_0)^{cor}$, (a) $\Delta = -6.7$ ppm or (b) $\Delta = 0$ ppm; black crosses, $(\Delta S/S_0)^{sim}$, (a) $\Delta = -6.7$ ppm or (b) $\Delta = 0$ ppm; red up triangles; $(\Delta S/S_0)^{cor}$, (a) $\Delta = -16.7$ ppm or (b) $\Delta = -12.0$ ppm; blue down triangles, $(\Delta S/S_0)^{sim}$, (a) $\Delta = -16.7$ ppm or (b) $\Delta = -12.0$ ppm.

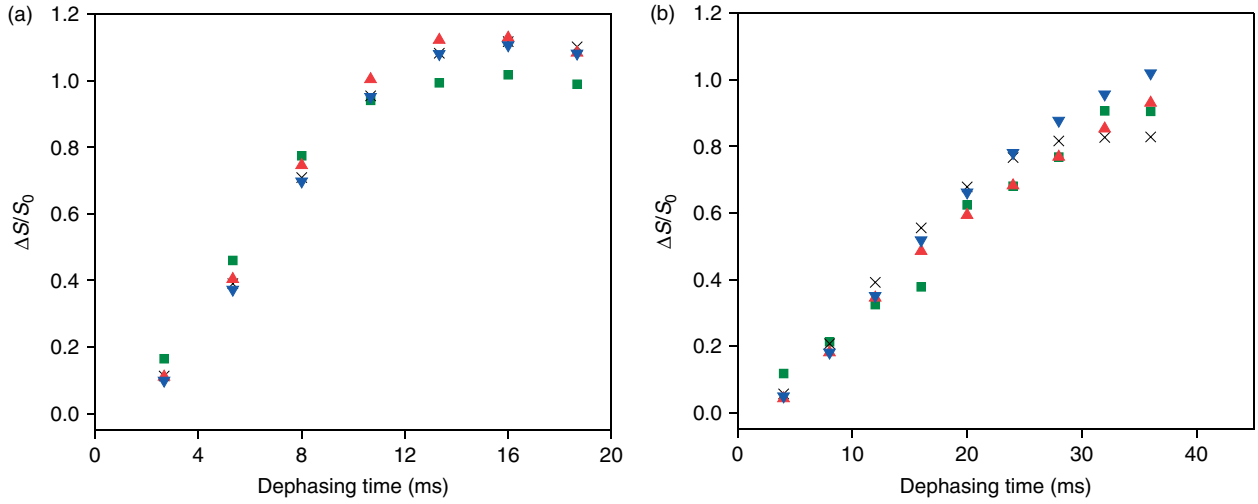

Figure 8. (a) D-NAL and (b) D-GFF plots of fpCTDQBU $(\Delta S/S_0)^{cor}$ and $(\Delta S/S_0)^{sim}$ *versus* dephasing time for ^{13}C π pulses with different nutation angles. Acquisition parameters included one-π-per-τ_R, MAS frequency = 12 000 Hz, 20.5 kHz ^{13}C π pulses, and (a) $\Delta = -6.7$ ppm, $CT = 20.00$ ms or (b) $\Delta = 0$ ppm, $CT = 41.33$ ms. The numbers of scans, integration parameters, and calculation of $(\Delta S/S_0)^{sim}$ were the same as in Fig. 7. The ^{13}C nutation angle is denoted θ. The symbol legend: green squares, $(\Delta S/S_0)^{cor}$, $\theta = 180°$; red up triangles; $(\Delta S/S_0)^{sim}$, $\theta = 180°$; black crosses, $(\Delta S/S_0)^{sim}$, (a) $\theta = 170°$ or (b) $\theta = 175°$; blue down triangles, $(\Delta S/S_0)^{sim}$, (a) $\theta = 190°$ or (b) $\theta = 185°$.

180°, or 190° while for D-GFF, there was some variance of the $(\Delta S/S_0)^{sim}$ calculated for $\theta = 175°$, 180°, or 185°. The D-GFF $(\Delta S/S_0)^{sim}$ calculated with $\theta = 175°$ were subsequently considered as an 'experimental' data set and were fitted to $(\Delta S/S_0)^{sim}$ calculated with $\theta = 180°$ and different values of d. The new best-fit d was ~10% different from the value originally determined using the $(\Delta S/S_0)^{cor}$ values. A similar variance was obtained when fitting $(\Delta S/S_0)^{sim}$ calculated with $\theta = 185°$.

Fitting of HFP fpCTDQBU data

For the HFPtr-A15 sample, Fig. 5(a) shows that $(\Delta S/S_0)^{cor} \approx 0$ for $\tau < 35$ ms and comparison with simulations suggested an upper limit of ~15 Hz on d or a lower limit of ~8 Å on r. The HFPmn-F8 and the HFPtr-A6 samples both had fairly rapid buildup of $(\Delta S/S_0)^{cor}$ calculated with $h = 1$, i.e. all labeled ^{13}CO were considered to have the same value of d. However, the $(\Delta S/S_0)^{cor}$ at large τ were between 0.4 and 0.6 and these values were about half of the expected

DOI: 10.1002/mrc

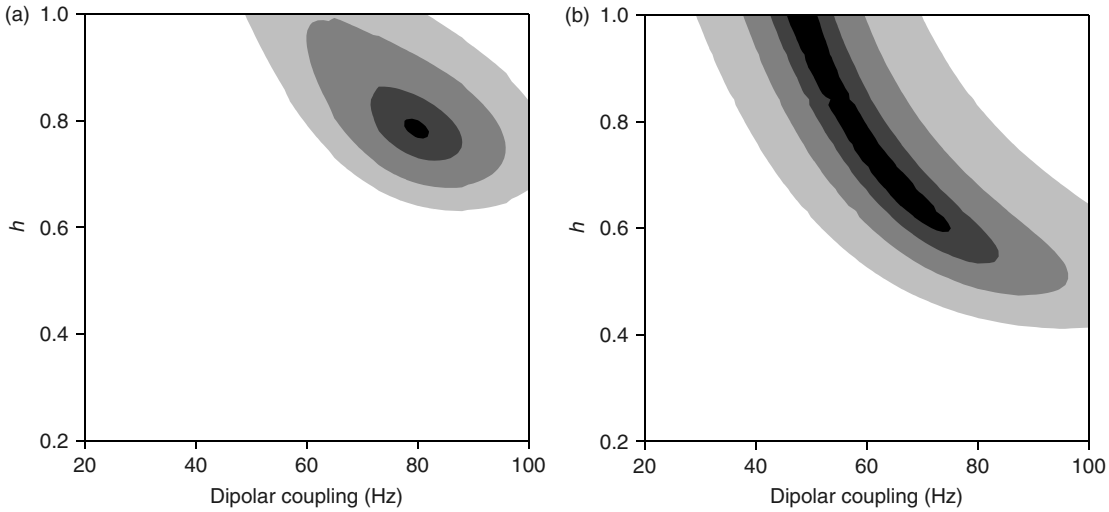

Figure 9. Contour plots of χ^2 for membrane-associated (a) HFPmn-F8 and (b) HFPtr-A6. The χ^2 were calculated with comparison of $(\Delta S/S_0)^{cor}$ and $(\Delta S/S_0)^{sim}$ calculated with a two-parameter model. For this model, there was a population fraction (h) of labeled ^{13}C which experienced measurable $^{13}C-^{13}C$ dipolar coupling and a population fraction $(1-h)$ of labeled ^{13}C which experienced no $^{13}C-^{13}C$ dipolar coupling. The horizontal and vertical axes are the measurable dipolar coupling and h parameters, respectively. The shading legend: black, (a) $1.0 < \chi^2 < 1.1$ or (b) $6 < \chi^2 < 7$; dark gray, (a) $1.1 < \chi^2 < 2.0$ or (b) $7 < \chi^2 < 10$; gray, (a) $2 < \chi^2 < 5$ or (b) $10 < \chi^2 < 20$; light gray, (a) $5 < \chi^2 < 10$ or (b) $20 < \chi^2 < 50$; white, (a) $\chi^2 > 10$ or (b) $\chi^2 > 50$.

$(\Delta S/S_0)^{sim}$ (*cf* Fig. 4(a)). As noted in Eqn (7), this discrepancy could be reduced with a two-population model in which a fraction (h) of the labeled ^{13}CO experienced a single nonzero value of d and a fraction $(1-h)$ experienced $d = 0$. For the HFPmn-F8 data, $\chi^2(d, h)$ was determined using $(\Delta S/S_0)^{cor}$ calculated for $0.2 \leq h \leq 1$ and $(\Delta S/S_0)^{sim}$ calculated for $20\,Hz \leq d \leq 100\,Hz$, *cf* Fig. 9(a). The χ^2 contour plot had a well-defined minimum centered at $h = 0.78$ and $d = 80\,Hz$ ($r = 4.6\,Å$) and the most likely d and h were within the black and dark gray regions of this plot.[58] A similar analysis was done for the HFPtr-A6 data and yielded best-fit parameter values $h = 0.99$ and $d = 49\,Hz$ ($r = 5.4\,Å$), *cf* Fig. 9(b). The black and dark gray good-fit regions had a curved shape that approximately extended from the best-fit parameter values to $h \approx 0.5$ and $d \approx 80\,Hz$ ($r = 4.6\,Å$).[67]

DISCUSSION

Over the past 20 years, there have been significant methodological advances in measurement of $^{13}C-^{13}C$ dipolar couplings under MAS.[1,2] This paper includes investigation of two related methods for these measurements which are based on rotor-synchronized finite ^{13}C π pulses, i.e. pulses which are a significant fraction of a rotor period.[17,20,21] Strengths of these sequences include the following: (i) nearly all pulses are π pulses with quadrature phases; (ii) the sequences are amenable to measurements on samples with inexpensive ^{13}CO labeling; (iii) the setup is straightforward and rapid; and (iv) the data are relatively insensitive to chemical shifts and CSA including the relative orientations of the dipolar and chemical shift tensors.[19,21,22] Use of finite rather than short π pulses in CTDQBU led to more rapid buildup of $\Delta S/S_0$. In particular, fpRFDR is applicable to spin systems whose nuclei have similar chemical shifts and chemical shift tensor orientations such as ^{13}CO in β strands.[15,19] Much slower buildup is observed with short-pulse RFDR in this system.[22]

The *CT* aspect of fpCTDQBU allowed neglect of transverse relaxation in the data analysis but also led to reduced signal because of transverse relaxation during the long *CT* period. Versions of fpCTDQBU which incorporate shorter *CT* should therefore yield higher signal-to-noise data. Previous CTDQBU and fpCTDQBU studies had used the one-π-per-$2\tau_R$ version while in the present study, it was shown that the one-π-per-τ_R version led to more rapid buildup of $\Delta S/S_0$ presumably because there was a larger finite pulse effect.[17,19,22] For $r \sim 5\,Å$ and $d \sim 60\,Hz$, *CT* could be reduced by a factor of ~0.6 to ~40 ms, *cf* Figs 4(a), 5(a). The sensitivity improvement should be significant for samples such as membrane-associated HFPs which have $T_2 \sim 15$ ms. An additional advantage of the one-π-per-τ_R version was $(\Delta S/S_0)^{cor}$ and $(\Delta S/S_0)^{sim}$ of ~0.9 at large $d\tau$ as compared to ~0.75 for the one-π-per-$2\tau_R$ version, *cf* Fig. 4(a).[22] This study also showed that reasonable transmitter offsets and errors in the ^{13}C π pulse nutation angle reduced best-fit d by ~10% and the corresponding best-fit r by ~3%. This error is small compared to the variation in r among different HFP structural models and the method should therefore be useful for distinguishing among the models.

This paper also includes some investigation of the related fpRFDR-CT sequence for $^{13}C-^{13}C$ distance measurement in HFP samples. One advantage of the chosen version of fpRFDR-CT was its use of multiple WAHUHA cycles for refocusing of $^{13}C-^{13}C$ dipolar coupling rather than the solid echo used in fpCTDQBU.[25,26] In the context of average Hamiltonian theory, the solid echo only averages dipolar evolution for two spin 1/2 nuclei whereas WAHUHA averages dipolar evolution for multiple spin 1/2 nuclei.[55,56] Comparison of S_0 spectra between the two sequences for GFF indeed showed ~1.5 times higher signal for fpRFDR-CT. For this version of fpRFDR-CT, there was variation of the transverse relaxation period with τ but multiplication of

DOI: 10.1002/mrc

$(S_1/S_0)^{sim}$ by $exp(-\tau/3T_2)$ led to accurate determination of d and r in GFF which had $T_2 \approx 55$ ms. This simple approach to transverse relaxation correction was more problematic in the HFP samples because $T_2 \approx 15$ ms and the decay time constant of $(S_1/S_0)^{cor}$ with τ was comparable to $3T_2$. The shorter ^{13}CO T_2 appeared to be specific to membrane-associated HFP as previous reports of ^{13}CO and $^{13}CH_3$ T_2s in amyloid fibrils were ~50 ms.[21] Future studies might consider a different version of fpRFDR-CT which has a fixed transverse relaxation period and which uses a solid echo rather than WAHUHA for $^{13}C-^{13}C$ dipolar refocusing.[19] Another alternative is the recently developed PITHIRDS-CT sequence in which evolution or averaging of $^{13}C-^{13}C$ dipolar coupling is accomplished with different combinations of acquisitions which have different placements of the ^{13}C π pulses within the rotor cycles.[68]

One difference between the versions of fpCTDQBU and fpRFDR-CT presented in this paper was the acquisition of an S_0 spectrum for each τ in fpCTDQBU and acquisition of a single S_0 spectrum in fpRFDR-CT. This difference resulted in higher sensitivity for fpRFDR-CT. If S_0 were independent of τ for fpCTDQBU, data analysis could also be done with a single S_0 spectrum, but Fig. 6(b) showed ~20% variation of S_0 with maximum S_0 for $\tau \approx CT/2$ and minimum S_0 for $\tau \approx 0$ and $\tau \approx CT$. Considering $S_0(\tau) \approx F(\tau) \times F(CT - \tau)$ where $F(t)$ was the dipolar echo intensity, it appeared that $F(t)$ had a nonexponential decay component which caused greater signal loss at larger t. The variation of S_0 with τ was also qualitatively observed in simulations and could be reduced by using higher ^{13}C π pulse phase cycles such as XY-16 or XY-32.[54] Another possible solution is multiple short echo periods that would each contain a $(\pi/2)(\pi/2)$ pulse pair at the center of each period rather than a single long echo period with a single $(\pi/2)(\pi/2)$ pulse pair at the center of the period. The rationale for this approach is that the solid echo works better for smaller values of dipolar coupling times echo period.[55,56] The PITHIRDS-CT sequence might also be useful because it is based on the relative positions of π pulses in the rotor period rather than on solid echoes.[68]

Although improvements to the finite pulse-based methods should be possible as detailed in the previous paragraphs, the fpCTDQBU sequence in the form presented in this paper is already a useful method to investigate membrane-associated HFP strand arrangements. It was encouraging that significant differences were observed between the data of peptides labeled at different ^{13}CO sites, *cf* Fig. 5(a). An effort was made to understand the structural implications of these data with the caveat that data for peptides with other labeled sites will be needed to develop an unambiguous structural model. Although one sample was made with HFPmn and the other two were made with HFPtr, it was assumed that the variations of $(\Delta S/S_0)^{cor}$ among the samples were due to the different ^{13}CO labeled sites rather than the differences in cross-linking.

The interpretation was done in the context of β-sheet HFP models previously developed using solid-state NMR and infrared data.[22,47] In one model, adjacent HFP strands are parallel to one another and are in-register. Example hydrogen bonds between adjacent strands would be Ala-6 CO···HN Leu-7, Phe-8 CO···HN Leu-9, and Ala-15 CO···HN Gly-16. In this model, the distance between labeled ^{13}COs on adjacent strands is ~4.8 Å for the HFPtr-A6, HFPmn-F8, and HFPtr-A15 samples. In a second model, adjacent HFP strands are antiparallel to one another with strand crossing between Phe-8 and Leu-9. Example hydrogen bonds between adjacent strands are then Ala-6 CO···HN Phe-11, Phe-8 CO···HN Leu-9, and Ala-15 CO···HN Val-2. A key feature of the antiparallel model is the variation among the different samples of the distance between labeled ^{13}COs on adjacent strands, e.g. ~4.8 Å in HFPmn-F8 and ≥15 Å in HFPtr-A6 and HFPtr-A15.

The clearest data analysis could be done for the HFPmn-F8 sample, *cf* Fig. 9(a), and yielded best-fit $d \approx 80$ Hz, $r \approx 4.6$ Å, and $h \approx 0.8$. The best-fit distance was generally consistent with the predicted distances of either the parallel or the antiparallel model. For the parallel model, the same $d \approx 80$ Hz would be predicted for the HFPtr-A6 sample and the good-fit region of the χ^2 plot for this sample included $d \approx 80$ Hz with accompanying $h \approx 0.5$, *cf* Fig. 9(b). The antiparallel model predicted $r \approx 15$ Å and $d \approx 2$ Hz for HFPtr-A6 and was a poor fit to the data. The parallel strand arrangement did not appear to extend to Ala-15 as evidenced by $(\Delta S/S_0)^{cor} \approx 0$ for $\tau < 35$ ms in the HFPtr-A15 data, *cf* Fig. 5(a). The upper limit on d for this sample was ~15 Hz.

An overall HFP model consistent with the data in this study was: (i) a mixture of parallel and antiparallel strand arrangements in the region of HFP that included Ala-6 and Phe-8; and (ii) loss of parallel β-sheet structure in the Ala-15 region. Supporting evidence for point (i) included the larger h of the HFPmn-F8 sample relative to the HFPtr-A6 sample. This result correlated with: (i) the large d predicted by both parallel and antiparallel models for HFPmn-F8 and (ii) the large and small ds predicted for HFPtr-A6 by the parallel and antiparallel models, respectively. Previous measurements of interstrand homonuclear and heteronuclear dipolar couplings in HFP samples were also consistent with a mixture of parallel and antiparallel strands.[22,38]

As noted above, evidence for loss of parallel β-sheet structure near Ala-15 included $(\Delta S/S_0)^{cor} \approx 0$ for the HFPtr-A15 sample. This *C*-terminal 'fraying' of the parallel β sheet was also consistent with larger Ala-15 ^{13}CO linewidths and with previous measurements of interpeptide $^{13}CO-^{15}N$ dipolar couplings.[38] Previous studies have also shown that the Ala-15 ^{13}COs were in close 5–6 Å proximity to the ^{31}P in the lipid headgroups while distances between Ala-6 or Phe-8 ^{13}COs and lipid ^{31}Ps were >8 Å.[69] The combination of the different data suggests a general structural model in which: (i) residues in the apolar *N*-terminal region of HFP are located in the low water content acyl chain region of the membrane and form regular β-sheet structure and (ii) residues in the more polar *C*-terminal region are located in the lipid headgroup region and have greater structural disorder because of hydrogen bonding with water.[35]

CONCLUSIONS

This study demonstrated improved performance of the fpCTDQBU sequence using the one-π-per-τ_R version as well

DOI: 10.1002/mrc

as the robustness of the sequence to transmitter offsets and errors in the ^{13}C π pulse nutation angle. In addition, significant differences in fpCTDQBU data were observed for membrane-associated HFP labeled at different ^{13}CO sites and were interpreted with a model of mixed parallel and antiparallel β-strand arrangements in the *N*-terminal region of HFP and loss of parallel β-sheet structure in the *C*-terminal region of HFP. Future comparative ^{13}CO–^{13}CO distance measurements among different HFP constructs should elucidate variations in strand arrangements among the constructs and may be correlated to differences in their observed fusion rates.

Acknowledgements

This work was supported by NIH AI47153 and used resources at Michigan State University including the Max T. Rogers NMR facility, the mass spectrometry facility, and the Michigan Center for Biological Information LINUX cluster. Dr David DeWitt is acknowledged for use of his ultracentrifuge and Dr Yoshitaka Ishii and Dr Charles Gabrys are acknowledged for helpful discussions.

REFERENCES

1. Tycko R. *Annu. Rev. Phys. Chem.* 2001; **52**: 575.
2. Drobny GP, Long JR, Karlsson T, Shaw W, Popham J, Oyler N, Bower P, Stringer J, Gregory D, Mehta M, Stayton PS. *Annu. Rev. Phys. Chem.* 2003; **54**: 531.
3. Hong M. *Structure* 2006; **14**: 1731.
4. Tycko R, Dabbagh G. *Chem. Phys. Lett.* 1990; **173**: 461.
5. Lee YK, Kurur ND, Helmle M, Johannessen OG, Nielsen NC, Levitt MH. *Chem. Phys. Lett.* 1995; **242**: 304.
6. Hohwy M, Jakobsen HJ, Eden M, Levitt MH, Nielsen NC. *J. Chem. Phys.* 1998; **108**: 2686.
7. Rienstra CM, Hatcher ME, Mueller LJ, Sun BQ, Fesik SW, Griffin RG. *J. Am. Chem. Soc.* 1998; **120**: 10602.
8. Brinkmann A, Eden M, Levitt MH. *J. Chem. Phys.* 2000; **112**: 8539.
9. Nielsen NC, Bildsoe H, Jakobsen HJ, Levitt MH. *J. Chem. Phys.* 1994; **101**: 1805.
10. Gregory DM, Mehta MA, Shiels JC, Drobny GP. *J. Chem. Phys.* 1997; **107**: 28.
11. Carravetta M, Eden M, Zhao X, Brinkmann A, Levitt MH. *Chem. Phys. Lett.* 2000; **321**: 205.
12. Raleigh DP, Levitt MH, Griffin RG. *Chem. Phys. Lett.* 1988; **146**: 71.
13. Kristiansen PE, Carravetta M, van Beek JD, Lai WC, Levitt MH. *J. Chem. Phys.* 2006; **124**: 234510.
14. Bennett AE, Ok JH, Griffin RG, Vega S. *J. Chem. Phys.* 1992; **96**: 8624.
15. Bennett AE, Rienstra CM, Griffiths JM, Zhen WG, Lansbury PT, Griffin RG. *J. Chem. Phys.* 1998; **108**: 9463.
16. Gullion T, Vega S. *Chem. Phys. Lett.* 1992; **194**: 423.
17. Bennett AE, Weliky DP, Tycko R. *J. Am. Chem. Soc.* 1998; **120**: 4897.
18. Balazs YS, Thompson LK. *J. Magn. Reson.* 1999; **139**: 371.
19. Ishii Y. *J. Chem. Phys.* 2001; **114**: 8473.
20. Ishii Y, Balbach JJ, Tycko R. *Chem. Phys.* 2001; **266**: 231.
21. Balbach JJ, Petkova AT, Oyler NA, Antzutkin ON, Gordon DJ, Meredith SC, Tycko R. *Biophys. J.* 2002; **83**: 1205.
22. Zheng Z, Yang R, Bodner ML, Weliky DP. *Biochemistry* 2006; **45**: 12960.
23. Tseng YH, Mou Y, Mou CY, Chan JCC. *Solid State Nucl. Magn. Reson.* 2005; **27**: 266.
24. Waugh JS, Huber LM, Haeberlen U. *Phys. Rev. Lett.* 1968; **20**: 180.
25. Mehring M. *Principles of High-Resolution NMR in Solids*. Springer-Verlag: Berlin, New York, 1983.
26. Slichter CP. *Principles of Magnetic Resonance*. Springer Verlag: New York, 1992.
27. Hernandez LD, Hoffman LR, Wolfsberg TG, White JM. *Annu. Rev. Cell Dev. Biol.* 1996; **12**: 627.
28. Eckert DM, Kim PS. *Annu. Rev. Biochem.* 2001; **70**: 777.
29. Colman PM, Lawrence MC. *Nat. Rev. Mol. Cell Biol.* 2003; **4**: 309.
30. Freed EO, Myers DJ, Risser R. *Proc. Natl. Acad. Sci. U.S.A.* 1990; **87**: 4650.
31. Freed EO, Delwart EL, Buchschacher GL Jr, Panganiban AT. *Proc. Natl. Acad. Sci. U.S.A.* 1992; **89**: 70.
32. Pereira FB, Goni FM, Muga A, Nieva JL. *Biophys. J.* 1997; **73**: 1977.
33. Durell SR, Martin I, Ruysschaert JM, Shai Y, Blumenthal R. *Mol. Membr. Biol.* 1997; **14**: 97.
34. Martin I, Schaal H, Scheid A, Ruysschaert JM. *J. Virol.* 1996; **70**: 298.
35. Yang J, Gabrys CM, Weliky DP. *Biochemistry* 2001; **40**: 8126.
36. Aloia RC, Tian H, Jensen FC. *Proc. Natl. Acad. Sci. U.S.A.* 1993; **90**: 5181.
37. Brugger B, Glass B, Haberkant P, Leibrecht I, Wieland FT, Krasslich HG. *Proc. Natl. Acad. Sci. U.S.A.* 2006; **103**: 2641.
38. Yang J, Weliky DP. *Biochemistry* 2003; **42**: 11879.
39. Sackett K, Shai Y. *Biochemistry* 2002; **41**: 4678.
40. Chan DC, Fass D, Berger JM, Kim PS. *Cell* 1997; **89**: 263.
41. Tan K, Liu J, Wang J, Shen S, Lu M. *Proc. Natl. Acad. Sci. U.S.A.* 1997; **94**: 12303.
42. Weissenhorn W, Dessen A, Harrison SC, Skehel JJ, Wiley DC. *Nature* 1997; **387**: 426.
43. Caffrey M, Cai M, Kaufman J, Stahl SJ, Wingfield PT, Covell DG, Gronenborn AM, Clore GM. *EMBO J.* 1998; **17**: 4572.
44. Yang ZN, Mueser TC, Kaufman J, Stahl SJ, Wingfield PT, Hyde CC. *J. Struct. Biol.* 1999; **126**: 131.
45. Yang R, Yang J, Weliky DP. *Biochemistry* 2003; **42**: 3527.
46. Yang R, Prorok M, Castellino FJ, Weliky DP. *J. Am. Chem. Soc.* 2004; **126**: 14722.
47. Sackett K, Shai Y. *J. Mol. Biol.* 2005; **350**: 790.
48. Benzinger TL, Gregory DM, Burkoth TS, Miller-Auer H, Lynn DG, Botto RE, Meredith SC. *Proc. Natl. Acad. Sci. U.S.A.* 1998; **95**: 13407.
49. Chang CD, Waki M, Ahmad M, Meienhofer J, Lundell EO, Haug JD. *Int. J. Pept. Protein Res.* 1980; **15**: 59.
50. Lapatsanis L, Milias G, Froussios K, Kolovos M. *Synthesis-Stuttgart* 1983; **8**: 671.
51. Waskowska A, Lukaszewicz K, Kuzmina LG, Strutshkov YT. *Bull. Pol. Acad. Sci., Ser. Sci. Chim.* 1975; **23**: 149.
52. Precigoux G, Cotrait M, Geoffre S. *Acta Crystallogr., Sect. C* 1986; **42**: 315.
53. Bodner ML, Gabrys CM, Parkanzky PD, Yang J, Duskin CA, Weliky DP. *Magn. Reson. Chem.* 2004; **42**: 187.
54. Gullion T, Baker DB, Conradi MS. *J. Magn. Reson.* 1990; **89**: 479.
55. Haeberlen U. *High Resolution NMR in Solids*. Academic Press: New York, 1976.
56. Schmidt-Rohr K, Spiess HW. *Multidimensional Solid-state NMR and Polymers*. Academic Press: San Diego, 1994.
57. Carr HY, Purcell EM. *Phys. Rev.* 1954; **94**: 630.
58. Bevington PR, Robinson DK. *Data Reduction and Error Analysis for the Physical Sciences*. McGraw-Hill: Boston, 1992.
59. Bak M, Rasmussen JT, Nielsen NC. *J. Magn. Reson.* 2000; **147**: 296.
60. Herzfeld J, Berger AE. *J. Chem. Phys.* 1980; **73**: 6021.
61. Ando S, Yamanobe T, Ando I, Shoji A, Ozaki T, Tabeta R, Saito H. *J. Am. Chem. Soc.* 1985; **107**: 7648.
62. Oas TG, Hartzell CJ, McMahon TJ, Drobny GP, Dahlquist FW. *J. Am. Chem. Soc.* 1987; **109**: 5956.
63. Naito A, Ganapathy S, Akasaka K, McDowell CA. *J. Chem. Phys.* 1981; **74**: 3190.
64. Facelli JC, Gu ZT, McDermott A. *Mol. Phys.* 1995; **86**: 865.
65. Longhi S, Czjzek M, Lamzin V, Nicolas A, Cambillau C. *J. Mol. Biol.* 1997; **268**: 779.
66. Zhang HY, Neal S, Wishart DS. *J. Biomol. NMR* 2003; **25**: 173.
67. Gabrys CM, Yang J, Weliky DP. *J. Biomol. NMR* 2003; **26**: 49.
68. Tycko R. *J. Chem. Phys.* 2007; **126**: 064506.
69. Qiang W, Yang J, Weliky DP. *Biochemistry* 2007; **46**: 4997.

DOI: 10.1002/mrc